CHALMERS
UNIVERSITY OF TECHNOLOGY

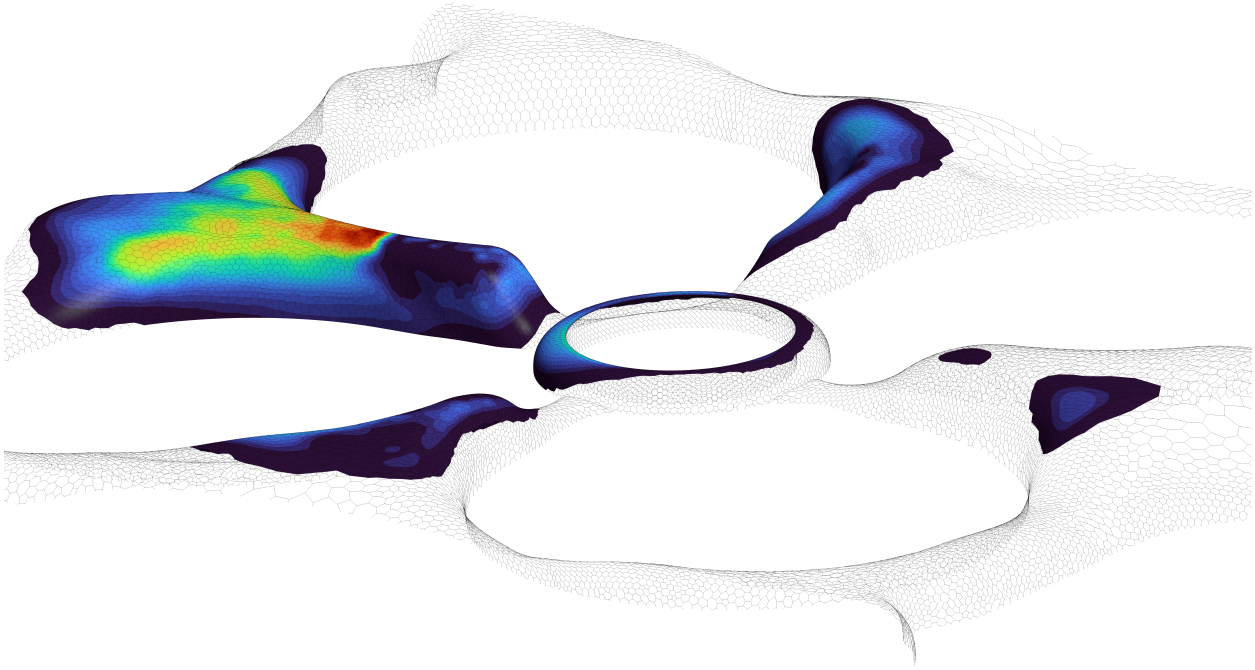

Modeling Nucleate Boiling in Engine Coolant Jacket

Analysis & Development of Semi-Mechanistic Boiling Methods in Heavy-Duty Diesel Engine Applications

Master's thesis in Applied Mechanics

Nils-Christian Bensryd
Aron Olofsson

DEPARTMENT OF MECHANICS AND MARITIME SCIENCES
CHALMERS UNIVERSITY OF TECHNOLOGY
Gothenburg, Sweden 2026
www.chalmers.se

Master's Thesis in Applied Mechanics

Modeling Nucleate Boiling in Engine Coolant Jacket

Analysis & Development of Semi-Mechanistic Boiling Methods in Heavy-Duty Diesel Engine Applications

Nils-Christian Bensryd
Aron Olofsson

CHALMERS
UNIVERSITY OF TECHNOLOGY

Department of Mechanics and Maritime Sciences
Division of Fluid Dynamics
Chalmers University of Technology
Gothenburg, Sweden 2026

Modeling Nucleate Boiling in Engine Coolant Jacket

Analysis & Development of Semi-Mechanistic Boiling Methods in Heavy-Duty Diesel Engine Applications

Nils-Christian Bensryd
Aron Olofsson

Supervisor:
Hampus Martinsson, Volvo TTI
Johan Abrahamsson, Volvo Penta
Sudharsan Vasudevan, Volvo TTI
Sassan Etemad, Adjunct Professor, Fluid Dynamics, Mechanics and Maritime Sciences / Volvo TTI
Examiner:
Niklas Andersson, Head of division, Fluid Dynamics, Mechanics and Maritime Sciences

Master's Thesis 2026
Department of Mechanics and Maritime Sciences
Chalmers University of Technology
SE-412 96 Gothenburg
Sweden
Telephone +46 31 772 1000

Cover: Visualization of predicted boiling heat flux in Simcenter STAR-CCM+, showing Cylinder 4 in the fluid domain. The image is included for illustration only. It does not represent the models used in this study for confidentiality reasons.

Typeset in LaTeX
Gothenburg, Sweden 2026

Modeling Nucleate Boiling in Engine Coolant Jacket

Analysis & Development of Semi-Mechanistic Boiling Methods in Heavy-Duty Diesel Engine Applications

Nils-Christian Bensryd
Aron Olofsson

Department of Mechanics and Maritime Sciences
Division of Fluid Dynamics
Chalmers University of Technology

Abstract

This thesis investigates subcooled nucleate boiling in a coolant jacket of a heavy-duty diesel engine, using a Conjugate Heat Transfer - Computational Fluid Dynamics (CHT-CFD) framework. As modern engines operate at increasingly high thermal loads under strict efficiency and emissions requirements, an accurate prediction of local cooling performance is essential. In cast-iron heavy-duty diesel engines, regions exposed to high thermal loads may experience nucleate boiling, which can enhance heat transfer if controlled, but may also lead to deterioration of cooling performance if excessive boiling occurs.

The work focuses on the implementation, calibration and validation of the Blended Boiling Model (BBM) and an extended Dry-spot Blended Boiling Model (DBBM) in STAR-CCM+ for two heavy-duty diesel engine variants. The models are evaluated in both a simple academic framework and a complete engine simulation framework, both validated with relevant experimental data. Their performance is also compared with that of other boiling models available in STAR-CCM+.

The results show that both BBM and DBBM predict boiling heat flux with reasonably good accuracy. The BBM performs well in the partial boiling regime and provides a useful indication of boiling intensity with a parameter called probability of bubble interactions. However, under low pressure and low coolant mass flow conditions, where the occurrence of a transition from nucleate boiling to film boiling is evident in the experiments, the BBM underestimates the wall temperatures. By introducing a dry-spot probability, the DBBM extends the modeling capability into more severe boiling regimes and improves the prediction in regimes where excessive boiling is observed in the experiments.

Keywords: CFD, STAR-CCM+, subcooled flow, nucleate boiling, Film boiling, heat transfer, multiphase flow

Preface

This report presents the outcome of our master's thesis project carried out at the Department of Mechanics and Maritime Sciences at Chalmers University of Technology during the spring of 2026.

Acknowledgements

We express sincere gratitude to our supervisors Hampus Martinsson, Johan Abrahamsson, Sudharsan Vasudevan and Sassan Etemad for their guidance, support and valuable feedback throughout this thesis. Their knowledge, encouragement and continuous engagement have been essential to the completion of this work. We would also like to extend our appreciation to Aurora De Leon for the opportunity to carry out this thesis work. In addition, we would like to thank Aristotelis Babajimopoulos for the extra assistance. We are also grateful to our examiner, Niklas Andersson, for valuable feedback and guidance during the thesis process. Finally, we would like to thank friends and colleagues for their support, their presence has made this journey more enjoyable and rewarding.

Nils-Christian Bensryd, Aron Olofsson, Gothenburg, February 2026

List of Acronyms

Below is the list of acronyms that have been used throughout this thesis listed in alphabetical order:

BBM	Blended Boiling Model
BDL	Boiling Departure Lift-off
CFD	Computational Fluid Dynamics
CHF	Critical Heat Flux
CHT	Conjugate Heat Transfer
DBBM	Dry-spot Blended Boiling Model
DNB	Departure from Nucleate Boiling
EGR	Exhaust Gas Recirculation
EG/W	Ethylene Glycol-Water
FCHT	Forced Convection Heat Transfer
FDB	Fully Developed Boiling
HDD	Heavy-Duty Diesel
HTBB	Heat-Transfer-Based Boiling
LC	Lemmert-Chawla
MP	Multiphase
ONB	Onset of Nucleate Boiling
RPI	Rensselaer Polytechnic Institute
SP	Single-Phase

Nomenclature

Below is the nomenclature of parameters and subscripts that have been used throughout this thesis.

Parameters

T	temperature [K]
ΔT	temperature difference [K]
σ	surface tension [N/m]
μ	dynamic viscosity [Pa s]
ν	kinematic viscosity [m^2/s]
ρ	density [kg/m^3]
h	specific enthalpy [J/kg]
h_{fc}	forced convection heat transfer coefficient [$W/(m^2\,K)$]
h_{nb}	nucleate boiling heat transfer coefficient [$W/(m^2\,K)$]
h_{lv}	latent heat of vaporization [J/kg]
k_l	thermal conductivity of liquid [W/(m K)]
k_g	thermal conductivity of gas [W/(m K)]
c_p	specific heat [J/(kg K)]
Pr	Prandtl number [-]
Re	Reynolds number [-]
Nu	Nusselt number [-]
Ja	Jakob number [-]
q	heat flux [W/m^2]
$\dot{q}''$	wall heat flux [W/m^2]
$\dot{m}''$	mass flux [$kg/(m^2\,s)$]
N	nucleation site number density [$sites/m^2$]
A	area [m^2]

d	diameter [m]
r	bubble radius [m]
r_D	bubble departure radius [m]
r_L	bubble lift-off radius [m]
d_d	bubble departure diameter [m]
d_{avg}	average bubble diameter [m]
f	frequency [Hz]
t	time [s]
t_{evap}	evaporation time scale [s]
t_{cond}	condensation time scale [s]
t_w	time between bubble departure and the nucleation of the next bubble [s]
u	velocity [m/s]
w	relative velocity [m/s]
g	gravitational acceleration [m/s^2]
F	force [N]
F_D	drag force [N]
F_L	lift force [N]
F_B	buoyancy force [N]
F_G	bubble growth force [N]
C_D	drag coefficient [-]
C_L	lift coefficient [-]
C_s	wall correction constant [-]
C_{sf}	surface-fluid empirical constant [-]
Θ	inclination angle [rad]
θ	contact angle [rad or °]
α	thermal diffusivity [m^2/s]
α_v	vapor volume fraction [-]
$\bar{\alpha}_v$	reference vapor volume fraction [-]
Π_{int}	probability of bubble interaction [-]
Π_{dry}	probability of dry spot [-]
ω_{evap}	evaporation source term [s^{-1}]
ω_{cond}	condensation source term [s^{-1}]
$Su_{a,v}$	vapor volume fraction source term [s^{-1}]
$Su_{a,l}$	liquid volume fraction source term [s^{-1}]

$x_{v,eq}$	vapor mass fraction [-]
P	pressure [Pa]
L	length scale [m]
K_{cond}	condensation constant [-]
K_{quench}	quenching area factor [-]
F_A	area coefficient scaling [-]

Subscripts

sat	saturation
sub	subcooled
lv	latent heat of vaporization
fc	forced convection
nb	nucleate boiling
FDB	fully developed boiling
BDL	boiling departure lift-off
BBM	blended boiling model
$DBBM$	dry-spot blended boiling model
ONB	onset of nucleate boiling
int	interaction
dry	dry-spot
$conv$	convection / convective
$evap$	evaporation / evaporative
$cond$	condensation / condensing
$quench$	quenching
$wall$	wall
ref	reference
hyd	hydraulic
$bulk$	bulk
w	wall
b	bulk
s	saturation
l	liquid
v	vapor

g	gas
m	mixture

Contents

List of Figures

List of Tables

1

Introduction

The continuous demand for increased efficiency, smaller size, high-power density engines and reduced emissions in the modern automotive industry has led to increasingly compact engine designs operating under elevated thermal loads. The need for highly effective cooling systems is necessary to keep component temperatures within acceptable limits to ensure engine durability and life expectancy. In liquid-cooled combustion engines, heat removal is often achieved with intended convective cooling within the coolant jacket.

Heavy-duty Diesel engines are made from cast-iron compared to other automotive applications, e.g. aluminum for passenger car engines. They operate at higher thermal loads, increasing the necessity for efficient cooling. In high specific-power engines, nucleate boiling often occurs unintentionally in regions exposed to high thermal loads. To a further extent, this can lead to film boiling, which has devastating consequences for engine components. The conventional approach has therefore been to suppress this type of boiling by increasing the coolant flow rate, the system pressure or a combination thereof. This strategy prevents any form of boiling and thus does not explore the potential for increased heat transfer and the benefits of controlled nucleate boiling.

Nucleate boiling is the vaporization of the liquid coolant in the form of vapor bubbles on the heated surface when the surface temperature exceeds the saturation temperature of the liquid. Nucleate boiling can be categorized into different regimes. The regimes are; isolated bubbles, partially developed boiling, fully developed boiling, transition boiling, and film boiling. Increasing the surface temperature to a few degrees above the saturation temperature leads to vapor formation on the heated surface in the superheated region of the fluid close to the wall. Nucleate boiling can be categorized into pool- and flow boiling depending on whether the liquid is static or in motion. Nucleate boiling enhances heat transfer through increased mixing and latent heat transport. This mechanism can significantly improve local cooling. Excessive boiling may lead to bubbles coalescing into a continuous vapor layer at the heated surface, often referred to as dry-out, which drastically reduces heat transfer. This is due to the low thermal conductivity of the vapor film at the heated surface. This phenomenon is called film boiling, which could result in local overheating and potential damage to engine components.

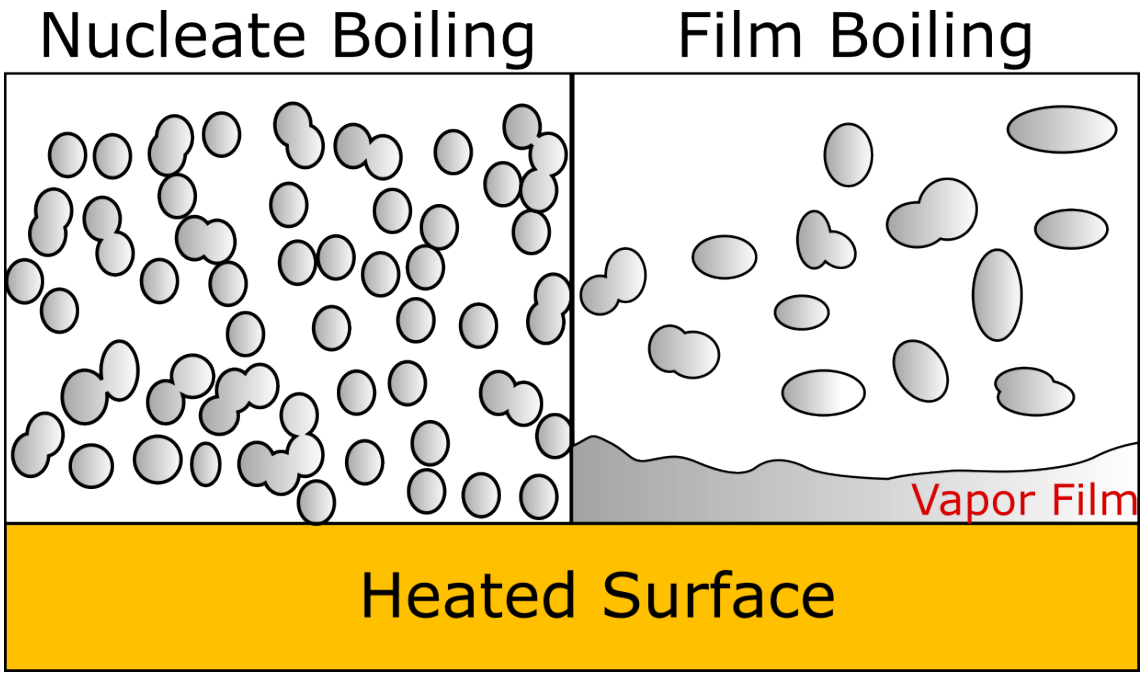

Figure 1.1: For the same substrate and boiling fluid, two different conditions: Nucleate boiling and Film boiling, respectively.

Modeling this process can be difficult because the boiling process is inherently complex and depends on multiple parameters, such as velocity, pressure, temperature, material-liquid combinations etc., which are still not fully understood. To quote Steiner et al. [1]:

> *"A realistic, physically sound model description of nucleate boiling flow is still challenged by very fundamental difficulties, as this highly complex phenomenon involves many sub-processes which are not fully understood yet"*

Therefore, the objective of this thesis is to develop, validate and extend the capabilities of existing models on a CFD-CHT based model for predicting subcooled nucleate boiling in diesel engine coolant jackets under different operating conditions. The work focuses on implementing a semi-mechanistic wall boiling model to estimate boiling heat flux, assessing single-phase and different mixture-multiphase models in terms of accuracy and computational cost and validating the approach against dedicated experiments and engine test-rig measurements. Finally, the validated models are used to identify regions and operating conditions with an increased risk of excessive boiling and to propose safe limits for controlled nucleate boiling without the risk of film boiling.

1.1 Background

The general approach has been to validate boiling models on simple geometries with experiments and then further implement the models in a CFD-CHT simula-

tion framework of an internal combustion engine. Punekar and Das [2] used Chen's boiling model [3] within a CFD-CHT framework. Shala [4] has used the Rensselaer Polytechnic Institute (RPI) boiling model proposed by Kurul and Podowski [5] using a mass transfer model when accounting for the presence of the vapor phase within a mixture multiphase model. Hua et al. [6] also used the RPI boiling model in a two fluid Eulerian approach in a CHT framework. Finlay et al. [7] experimented with a 50% volume mixture of EG/W in a uniformly heated cylindrical duct to investigate subcooled flow boiling using different materials such as copper, aluminum and cast-iron. They concluded that nucleate boiling can have a significant influence on heat transfer, particularly at velocities below 1.0 m/s. Ramstorfer et al. [8] investigated subcooled flow boiling heat transfer with different types of coating applied to cast-iron surfaces in a vertical test channel, using a 40/60 EG/W composition. The results demonstrated that the heated surface can significantly influence the intensity of boiling heat transfer due to the modified microstructure after coating. Chen et al. [9] studied the effects of bubble growth with microlayer evaporation using numerical methods and found a greater rate of microlayer evaporation with a higher thermal conductivity of the heat transfer surface.

The boiling models discussed in the aforementioned studies predict the intensity of boiling under specific thermal and flow conditions. However, they rarely account for the total extent of boiling relative to an upper limit, which is necessary to prevent transitions to film boiling regimes. The paper by Vasudevan et al. [10] created a boiling model for the local nucleate boiling effect based on Poisson distributions. The model is built using a semi-mechanistic approach aimed at capturing the multiple phenomena involved in nucleate boiling. The blended boiling model (BBM) was based on internal combustion engines for commercial automotive vehicles constructed from aluminum. The Blended Boiling Model (BBM), in conjunction with a CFD-CHT simulation framework for internal combustion engines, can predict boiling heat flux given thermal and flow conditions. The probability parameter (Π_{int}) used in the model, which indicates vapor bubble interaction, can also be used for conservatively quantifying the risk of film boiling.

1.2 Purpose

The primary aim of this work is to adapt and implement the BBM, within a CHT framework for a heavy-duty diesel engine in the CFD code, STAR-CCM+. This involves implementing the model in a multiphase framework and comparing it with FCHT (no boiling), single-phase and multiphase framework model alternatives, as well as experimental values. Secondarily, propose improvements to the model to better predict boiling within an HDD framework.

1.3 Goals

- Implement the boiling model for an academic baseline case for calibration.

- Implement the boiling model within an existing engine CFD-CHT simulation framework.
- Compare the proposed model with existing boiling models available in STAR-CCM+.
- Calibrate the model parameters using the available experimental data from baseline and engine tests.
- Investigate the influence of operating parameters: coolant pressure, flow rate and bulk temperature.
- Investigate the ability of the models to estimate the risk of film boiling.
- Extend the proposed model to account for the effects of dry-spots.

1.4 Limitations / Demarcations

The study focuses on steady-state CFD simulations of the coolant-side boiling phenomena within the engine cooling jacket. Structural deformation, long-term material degradation, and combustion-side thermal fluctuations are beyond the scope of this work. Model validation is limited to published experimental data and in-house engine test data. Furthermore, transient engine operating cycles are not considered in the present study.

2
Theory

2.1 Subcooled Boiling Flow

When a surface is heated above the saturation temperature of the liquid, boiling is initiated. When the bulk temperature equals the saturation temperature, it results in boiling known as saturated boiling, where no condensation occurs. Subcooled boiling is defined as boiling that occurs when the bulk liquid temperature is below the saturation temperature. The vapor bubbles formed due to nucleate boiling on the heated surface condense when they come into contact with the subcooled liquid bulk, making the bubbles concentrate close to the heated surface.

Compared to convective heat transfer, i.e. conditions without the occurrence of boiling, subcooled boiling flow involves different phenomena that enhance heat transfer in the system. Nucleate boiling can be categorized into two subgroups: pool boiling and flow boiling. Pool boiling is known as boiling in which the liquid bulk remains stationary, and the heat transfer is a combination of natural convection and nucleate boiling. In contrast to pool boiling, when boiling occurs in forced flow, forced convection dominates and the boiling is delayed.

Nucleate boiling occurs in the superheated region close to the surface, where the temperature is above the saturation temperature. This is further delayed in flow boiling, where the forced flow suppresses nucleate boiling. The temperature must then reach the Onset Nucleate Boiling temperature (T_{ONB}) before it starts to boil. This temperature is derived using the criterion for onset nucleate boiling from Sato and Matsumura [11]

$$\Delta T_{sat,ONB} = \frac{4\sigma T_{sat} v_{lv} h_{fc}}{k_l h_{lv}} \left[1 + \left(\frac{k_l h_{lv} \Delta T_{sub}}{2\sigma T_{sat} v_{lv} h_{fc}} \right)^{1/2} \right] \tag{2.1}$$

Where ΔT_{sub} is the temperature difference between the temperature of the subcooled liquid and the saturation temperature.

Several mechanisms of heat transfer and fluid flow can be observed in subcooled boiling. Based on the occurrence of one or more of these mechanisms, different boiling regimes are identified within subcooled boiling. These regimes can be represented on a boiling curve shown in the figure 4.22, where the y-axis is logarithmic. AB is the single-phase regime, driven only by natural or forced convection. The wall temperature at this point has yet to reach the ONB and no boiling has occurred yet.

With increasing wall temperature, boiling becomes prevalent as isolated bubbles can be observed in the BB' section. The boiling curve starts to diverge from forced convection heat transfer (FCHT), and the heat transfer rate increases exponentially. The curve reaches partial boiling in $B'C$, the bubbles are dense enough for bubble interaction and can no longer be assumed to be fully isolated. In the region CD, the flow has reached fully developed boiling, where the heat transfer mechanisms are similar to that of pool boiling. With further increase in wall temperature, the system experiences maximum heat flux, known as Critical Heat Flux (CHF). Any further increase in temperature results in Departure from nucleate boiling (DNB). Past the CHF, in the region DE, The boiling has reached transition boiling, where vapor bubbles has increased in such amounts, that they build a film on the wall, reduces the liquid contact to the wall. The Vapor film acts as an insulator between the liquid and the solid thus reducing the heat flux. In EF, the heated surface is fully covered by the vapor film. This regime is called film boiling and is mostly driven by the forced convection of the vapor. This occurs for a wall temperature controlled system, whereas for a heat flux controlled system, at the CHF, the flow directly results in film boiling along DD'.

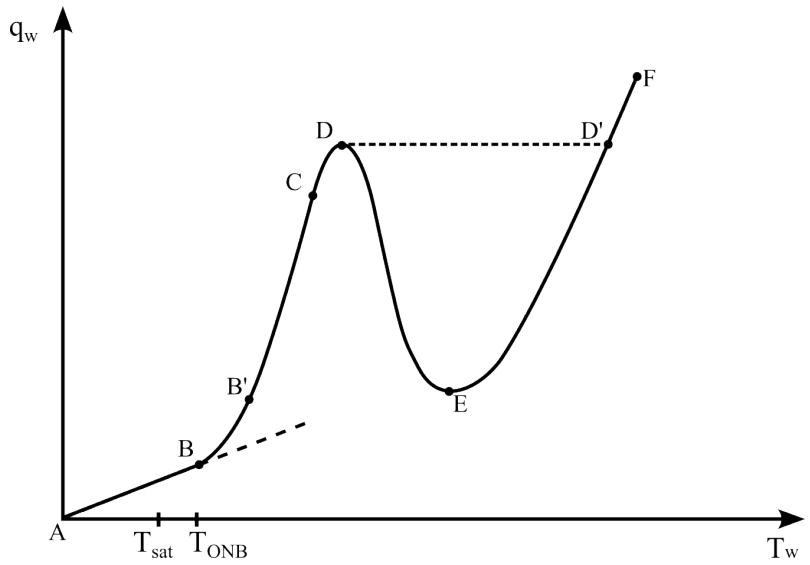

Figure 2.1: Boiling Curve showing the different Regimes from A-F

2.2 Numerical Boiling Models

Because of the complexity of subcooled flow boiling, the heat flux needs to be numerically modeled. Numerical models use a combination of mechanistic and empirical approaches to estimate heat flux in different regimes.

2.2.1 Rohsenow Pool Boiling Correlation

The well-established Rohsenow's correlation [12] was developed empirically to estimate the wall heat flux in pool boiling. Since the Fully Developed Boiling (FDB) regime is similar to pool boiling, Rohsenow's correlation is accurate within that

regime.

The expression for Rohsenow's correlation is defined as:

$$q_{FDB} = \mu_l h_{lv} \sqrt{\frac{g(\rho_l - \rho_v)}{\sigma}} \left(\frac{c_l \Delta T_{sat}}{C_{sf} h_{lv} Pr_l^{n_p}} \right)^m \tag{2.2}$$

Where μ_l, ρ_l, c_l and Pr_l are the dynamic viscosity, density, specific heat and Prandtl number of the liquid, respectively. ρ_v is the vapor density, h_{lv} is the latent heat of vaporization and σ is the surface tension. C_{sf}, n_p and m are empirical parameters that depend on the heated surface-coolant material combination and the composition of the coolant mixture.

2.2.2 Boiling Departure Lift-off

The Boiling Departure Lift-off (BDL) model by Steiner et al. [13] is designed to approximate the wall heat transfer for subcooled flow by improving the classical Chen [3] approach which means that local flow properties are used instead of global bulk parameters, with a semi-mechanistic approach based on the dynamics of a single-vapor bubble. The BDL model uses a heat flux partitioning approach, which partitions two additive contributions: forced convection (q_{fc}), due to the motion of the liquid, and nucleate boiling (q_{nb}), due to the formation and interaction of vapor bubbles with the bulk liquid; and is defined as:

$$q_{BDL} = q_{fc} + q_{nb} \cdot S_{flow} S_{Sub} \tag{2.3}$$

Where the forced convection heat flux (q_{fc}) is defined as:

$$q_{fc} = h_{fc}(T_w - T_b) \tag{2.4}$$

Following Chen's proposal, q_{fc} is dependent on the difference between the wall- (T_w) and bulk temperatures (T_b), where h_{fc} is calculated using the Dittus-Boelter [14] equation.

$$Nu_{fc} = \frac{h_{fc} d_{hyd}}{\lambda_1} = 0.023 Re_1^{0.8} Pr_1^{0.4} \tag{2.5}$$

The nucleate boiling heat flux (q_{nb}) is defined as follows:

$$q_{nb} = h_{nb}(T_w - T_{sat}) \tag{2.6}$$

And it depends on the difference between the wall- (T_w) and saturation temperature (T_{sat}), where h_{nb} is obtained using a correlation from Forster and Zuber [15]:

$$h_{nb} = 0.00122 \frac{\lambda_1^{0.79} c_{p,1}^{0.45} \rho_1^{0.49}}{\sigma^{0.5} \mu^{0.29} h_{lv}^{0.24} \rho_g^{0.24}} \Delta T_{sat}^{0.25} \Delta p_s^{0.75} \tag{2.7}$$

For subcooled flow boiling, Klausner et al. [16] and Steiner et al. [13] observed the following mechanism that suppressed the boiling heat flux. The experiments resulted in two suppression factors; flow-induced suppression (S_{flow}) and subcooling induced suppression (S_{sub}). S_{flow} accounts for the inertial forces of the forced

flow, which prematurely detaches the growing bubbles from their nucleation sites. S_{sub} accounts for the condensation of the bubble tip, which is in contact with the subcooled liquid bulk.

Steiner [13] solves the static force balance of the bubble at the instant of departure and lift-off. From the force balance, the bubble radius of the two instances (departure, (r_D) and lift-off, (r_L)) can be determined. These radii can be expressed as a ratio to define the flow-induced suppression term (S_{flow}) as follows:

$$S_{flow} = \frac{r_D}{r_L} \tag{2.8}$$

In pool boiling, these radii are equal ($S_{flow} = 1$). However, as the bulk velocity increased, r_D decreased relative to r_L, thus reflecting how the flow suppresses bubble growth.

The model also accounts for the effects of subcooling with the factor (S_{sub}) based on the concept 'extrapolated superheat layer thickness' by Wiebe and Judd [17] and is defined as:

$$S_{sub} = \frac{T_w - T_{sat}}{T_w - T_b} \tag{2.9}$$

This, in turn, limits the size of bubbles since they cannot protrude beyond the superheated layer near the wall without condensing. Where T_w, T_b, T_{sat} are the wall, bulk and saturation temperatures, respectively.

2.2.2.1 Force Balance of a Departing Bubble

Two instants of a bubble departing are considered from the force balance. The instant of "departure" represents the bubble when it has reached the critical departure volume, V_D, where the bubble is detached from its nucleation site. The instant of lift-off is when the bubble reaches a volume large enough for the buoyancy effect to lift the bubble from the surface. The radii of these two instances are determined by solving the corresponding force balance equations at each respective instance.
The forces acting on the bubble at the instant of departure from its nucleation site can be expressed as the static force balance in the x- and y-directions, as given below.

$$\sum F_x = F_D + F_G \sin\Theta \tag{2.10}$$

$$\sum F_y = F_B + F_G \cos\Theta + F_L \tag{2.11}$$

Where F_D, F_L, F_B, F_G and Θ is the drag-, shear lift-, buoyancy force and inclination angle, respectively. It is assumed that inertial forces are negligible due to the small density ratio ($\frac{\rho_g}{\rho_l} << 1$) of the gas and liquid, and the surface tension forces are also neglected at the moment of departure. Figure 2.2 shows the relevant forces at departure schematically.

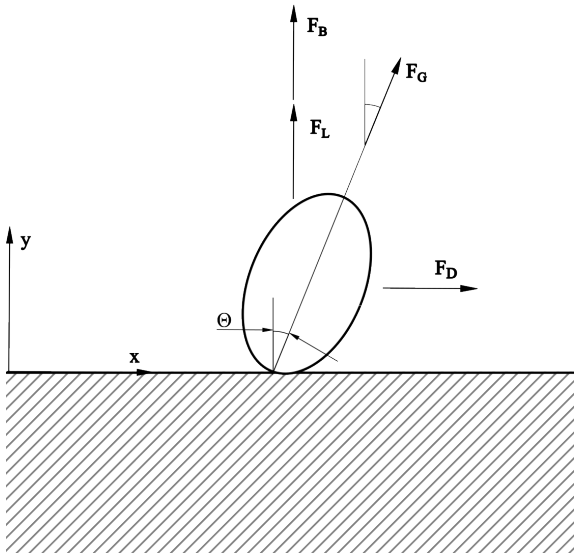

Figure 2.2: Force Balance of a departing bubble

During the instant of lift-off, it is assumed that there is no slip velocity. This assumption implies that zero drag and shear-lift force are set with a zero inclination angle. Therefore, the obtained force balance is defined as:

$$0 = F_B + F_G \tag{2.12}$$

Modeling of bubble forces has a few approaches which can be implemented. The chosen models were expressed by Steiner et al. [13] and Mazzocco et al. [18] respectively.

Steiner's approach
The bubble growth force, F_G, is modeled after a hemispherical bubble expanding in an inviscid liquid by Zeng et al. [19].

$$F_G = -\rho_l \pi r^2 \left(\frac{3}{2} C_s \dot{r}^2 + \ddot{r} \right) \tag{2.13}$$

Where the temporal evolution of the bubble radius is modeled assuming a diffusion controlled bubble growth model proposed by Zuber [20], Where b is an empirical constant.

$$r(t) = \frac{2b}{\sqrt{\pi}} Ja \sqrt{\alpha_l t} \tag{2.14}$$

Involving the Jakob number defined as:

$$Ja = \frac{\rho_l c_{p,l} (T_w - T_{sat})}{\rho_g h_{lv}} \tag{2.15}$$

Where α_l is the thermal diffusivity of the liquid, b is an empirical constant and $C_s = 20/3$ was introduced to account for the presence of the wall.

The drag (F_D) and shear lift forces (F_L) are defined as:

$$\begin{aligned} F_D &= 6\pi\mu_l u r \left\{ \frac{2}{3} + \left[\left(\frac{12}{Re_b} \right)^{0.65} + 0.796^{0.65} \right]^{-\frac{1}{0.65}} \right\} \\ F_L &= \frac{3.877}{2} \rho_l u^2 \pi r^2 G_s^{\frac{1}{2}} \left(\frac{1}{Re_B^2} + 0.014 G_s^2 \right)^{\frac{1}{4}} \end{aligned} \tag{2.16}$$

Where the bubble Reynolds number and shear rate are defined as:

$$\begin{aligned} Re_b &= \frac{\rho_l u 2r}{\mu_l} \\ G_s &= \left| \frac{du}{dy} \right|_{y=r} \frac{r}{u} \end{aligned} \tag{2.17}$$

The buoyancy force is given by.

$$F_B = \frac{4}{3} r^3 \pi g (\rho_l - \rho_g) \tag{2.18}$$

Mazzocco's approach
Mazzocco et al [18] developed a reassessed model for a more mechanistic prediction of bubble departure and lift off diameters and drag and shear lift forces are instead defined as:

$$F_D = \frac{1}{2} C_D \pi \rho_l w^2 r^2(t) \tag{2.19}$$

$$F_L = \frac{1}{2} C_L \pi \rho_l w^2 r^2(t) \tag{2.20}$$

The drag coefficient proposed by Zeng [19] for a solid sphere in a wall-bounded shear flow is modified according to Legendre and Magnaudet [21] to transition from a solid sphere to a bubble and is proposed as:

$$C_D \approx 1.13 \frac{24}{Re} (1 + 0.104 Re^{0.753}) \tag{2.21}$$

The lift coefficient is the upper-bound value for Stokes flow for a particle touching the wall, with a multiplier of 4/9 to account for the viscosity difference between materials inside and outside of the bubble interface.

$$C_L \approx \frac{4}{9} \cdot 5.87 \approx 2.61 \tag{2.22}$$

And the vapor bubble growth history is defined as:

$$r(t) = (K_{ML} + K_{FB}) t^{0.5} \tag{2.23}$$

Where the effects of micro-layer evaporation and heat transfer due to the surrounding fluid are superposed, the growth constant K_{ML} is from the works of Cooper et al [22] and is defined as:

$$K_{ML} = 2 \frac{\pi^2 + 1}{\pi^2 \sqrt{\pi}} \frac{1}{\sqrt{Pr_l}} Ja \sqrt{\nu_l} \tag{2.24}$$

And the growth constant K_{FB} is defined as:

$$K_{FB} = \chi K_{PB} \tag{2.25}$$

Where K_{PB} is from the works of Plesset and Zwick [23]:

$$K_{PB} = 2\sqrt{\frac{3}{\pi}} Ja \sqrt{\nu_l} \tag{2.26}$$

And $\chi = A - B\zeta$ is a simple functional form to account for both saturated and sub-cooled flow, where $A = 1.55$ and $B = 0$ are used for saturated flow and $A = 0$ and $B = 0.05$ for sub-cooled flow, respectively. Where ζ is defined as:

$$\zeta = \frac{T_{sat} - T_{bulk}}{T_w - T_{sat}} \tag{2.27}$$

Assuming a spherical bubble and the presence of the wall, the displacement of the liquid due to the bubble growth is approximately double that of a bubble far from the wall and thus:

$$F_G = 2F_G^{hem} \tag{2.28}$$

With Rayleigh-Plesset [23] treatment, we express the following:

$$F_G^{hem} = \frac{1}{8}\pi\rho_l K^4 \tag{2.29}$$

2.2.3 Blended Boiling Model

The Blended Boiling Model (BBM), proposed by Vasudevan et al. [24], blends the Rohsenow and BDL models by introducing a probability factor (Π_{int}) that is based on the number of active bubble nucleation sites and their distribution on the heated surface, which reads:

$$q_{BBM} = (1 - \Pi_{int}) \cdot q_{BDL} + \Pi_{int} \cdot q_{FDB} \tag{2.30}$$

The BDL model is intended for the isolated bubbles regime, where the bubbles are sparse and do not interact with each other. However, as the heat load increases, the system eventually transitions into the FDB regime, where the population of bubbles increases and they start to coalesce and interact. In this regime, the agitation caused by rapid bubble nucleation makes the effect of bulk flow velocity on boiling heat transfer negligible and the system behaves similarly to pool boiling. The transition between these two regimes is managed by Π_{int} and acts as a blending parameter. It is defined as a Poisson distribution:

$$\Pi_{int} = 1 - e^{-NA} \tag{2.31}$$

The blending parameter (Π_{int}) is defined as the probability of bubble interaction, which estimates the occurrence of more than one vapor bubble nucleating on the heated surface within the reference area (A) of two bubble departure diameters. The reference area is then defined as:

$$A = \pi d_{avg}^2 \tag{2.32}$$

Where the average bubble diameter is expressed based on the bubble departure diameter given by the force balance equations 2.10 and 2.11:

$$d_{avg} = \frac{2}{3} d_d = \frac{2}{3} 2 r_d \tag{2.33}$$

2.2.3.1 Nucleation Site Number Density

The number density of active nucleation sites, (N), is estimated by the model proposed by Li et al. [25] and reads:

$$N = N_0 \cdot f_1(\theta) \cdot f_2(P) \cdot f_3(\Delta T_{sat}) \tag{2.34}$$

With:

$$\begin{aligned} f_1(\theta) &= 1 - \cos\theta \\ f_2(P) &= e^{f(P)} \\ f_3(\Delta T_{sup}) &= \Delta T_{sat}^{A\Delta T_{sat}+B} \end{aligned} \tag{2.35}$$

And:

$$\begin{aligned} 1 - \cos\phi &= (1 - \cos\phi_0) \left(\frac{T_c - T_{sat}}{T_c - T_0} \right)^{\gamma} \\ f(P) &= 26.006 - 3.678 e^{-2P} - 21.907 e^{\frac{-P}{24.065}} \\ A &= -0.0002 P^2 + 0.0108 P + 0.0119 \\ B &= 0.122 P + 1.988 \end{aligned} \tag{2.36}$$

Where N_0 is an empirical constant used to scale the number of sites/m^2 and f_1, f_2 and f_3 are functions of contact angle, pressure and wall superheat, respectively. P is the pressure (in MPa), θ is the contact angle, T_c is the critical temperature and γ is a temperature-independent empirical constant

2.2.4 Dry-spot Blended Boiling Model

The applicability of the original BBM can be extended into the transitional boiling regime by introducing a mechanism to represent the deterioration of heat transfer associated with the emergence of dry-spots at the heated wall. This is achieved by defining an additional probability term for the occurrence of multiple interacting bubbles within a given surface area, representing the local accumulation of vapor bubbles near the wall.

The underlying assumption is that dry-spot formation becomes increasingly likely when the number of active nucleation sites within a characteristic area exceeds a critical value. This probability can be modeled using a Poisson distribution, similar to the probability of bubble interaction used in the BBM, but with a higher threshold corresponding to a critical active site number. In this way, the model estimates the likelihood of vapor crowding sufficient to locally hinder liquid replenishment to

the wall.

To account for the associated degradation in heat transfer, the wall heat flux is blended between a wet boiling contribution and a dry heat transfer contribution. The wet contribution is represented by the BBM heat flux (q_{BBM}), whereas the dry contribution is represented by the vapor-side heat flux (q_{dry}). The blending is controlled by the dry-spot probability, Π_{dry}, which allows the model to approximate the rapid reduction in heat transfer as the wall transitions towards partial dryout, as follows:

$$\Big[(1-\Pi_{int})\cdot q_{BDL}+\Pi_{int}\cdot q_{FDB})\Big]\cdot(1-\Pi_{dry})+q_{dry}\cdot\Pi_{dry} \tag{2.37}$$

Where q_{dry} is defined as the average Nusselt number for laminar flow over a flat plate for vapor:

$$\begin{aligned} q_{dry} &= \frac{Nu_g\cdot k_g}{L}\left(T_w-T_g\right) \\ Nu_g &= 2\cdot 0.332 Re_g^{1/2} Pr_g^{1/3} \end{aligned} \tag{2.38}$$

Where Re_g, Pr_g, k_g and L are the Reynolds number, Prandtl number, thermal conductivity and length scale for the vapor phase, respectively. The T_w and T_g is the wall- and gas temperatures, respectively.

The probability of dry-spot (Π_{dry}) is modeled after Ha and No [26], where it is assumed that the probability that the number of active site is greater than or equal to the critical active site number (n_c) that will be found in a shell area (A), is as follows:

$$\Pi_{dry}=P(n\geq n_c)=1-\sum_{n=0}^{n_c-1}\frac{(NA)^n}{n!}e^{-NA} \tag{2.39}$$

Assuming a critical active site number (n_c) of 4 and 5 illustrated in Figure 2.3, it is postulated that the bulk liquid can be supplied to the micro-layer under the bubble at the center for $n_c < 5$. Therefore in this present study, the critical number of bubbles considered for cutoff off liquid supply to the micro-layer is 5, (i.e $n_c = 5$).

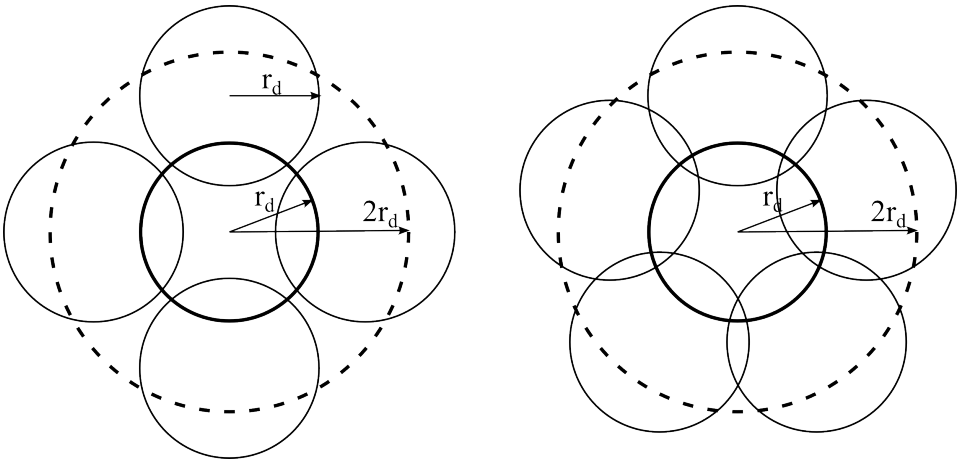

Figure 2.3: Illustration of a possible arrangement of critical active site number (n_c) of 4 & 5, respectively

2.2.5 Interphase Mass Transfer Model

Estimating the amount of liquid evaporation close to the wall and the amount of vapor condensing into the bulk liquid can be approximated by Bo [27]. Based on a mixture specific enthalpy (h_m), the reference vapor volume fraction ($\bar{\alpha}_v$), assuming a reduced thermal equilibrium condition as:

$$\bar{\alpha}_v = \frac{x_{v,eq}^n}{x_{v,eq} + (1 - x_{v,eq})^{\frac{\rho_v}{\rho_l}}} \tag{2.40}$$

Where the $x_{v,eq}$ is the mass fraction of vapor with $n = 1.1$ and is defined as:

$$x_{v,eq} = \begin{cases} 0, & h_m \leq h_{l,sat} \\ \frac{h_m - h_{l,sat}}{h_{lv}}, & h_{l,sat} \leq h_m \leq h_{v,sat} \\ 1, & h_m \geq h_{v,sat} \end{cases} \tag{2.41}$$

Where $h_{l,sat}$ and $h_{v,sat}$ are the saturation enthalpies of the liquid- and vapor phases respectively. And h_{lv} is the latent heat of vaporization. The saturation enthalpies are defined as:

$$\begin{aligned} h_{l,sat} &= h_{l,ref} + \int_{T_{ref}}^{T_{sat}} c_l dT \\ h_{v,sat} &= h_{v,ref} + \int_{T_{ref}}^{T_{sat}} c_v dT \\ h_{lv} &= h_{v,sat} - h_{l,sat} \end{aligned} \tag{2.42}$$

The difference between the actual computed vapor volume fraction (α_v) and the reference value ($\bar{\alpha}_v$) determines the driving force of evaporation or condensation and thus the source term is expressed as a summation of the two sources:

$$Su_{a,v} = \omega_{evap} + \omega_{cond} \tag{2.43}$$

Where ω_{evap} and ω_{cond} are volume fraction sources arising from evaporation or condensation. These are computed as:

$$\begin{aligned} \omega_{evap} &= \begin{cases} \frac{\bar{\alpha}_v - \alpha_v}{t_{evap}}, & \alpha_v < \bar{\alpha}_v \\ 0, & \alpha_v \geq \bar{\alpha}_v \end{cases} \\ \omega_{cond} &= \begin{cases} \frac{\bar{\alpha}_v - \alpha_v}{t_{cond}}, & \alpha_v > \bar{\alpha}_v \\ 0, & \alpha_v \leq \bar{\alpha}_v \end{cases} \end{aligned} \tag{2.44}$$

Where t_{evap} and t_{cond} are the time scales, and they are defined as:

$$\begin{aligned} t_{evap} &= 2.5 \\ t_{cond} &= K_{cond} \frac{T_{sat}}{\Delta T_{sub}} \end{aligned} \tag{2.45}$$

Where $K_{cond} = 5$ and the source term in the transport equation for volume fraction of the liquid ($Su_{a,l}$) is pf the opposite sign to the volume fraction source term of the vapor ($Su_{a,v}$):

$$Su_{a,l} = -Su_{a,v} \tag{2.46}$$

2.2.6 Rensselaer Polytechnic Institute Model

Heat-Transfer Based Boiling/Condensation model [28] is available in Star-CCM+ and is used for the mixture multiphase solver. It consists of both a Bulk and an optional wall boiling model. The Bulk boiling model is an interphase mass transfer model of the bulk liquid, dependent on the Nusselt number according to the user guide in Star-CCM+ [28]. The wall boiling model evaluates the boiling heat transfer and mass transfer developing on the wall. It implements Kurul's and Podowski's [5] model from the Rensselaer Polytechnic Institute. The model was therefore termed the RPI model.

The wall boiling model is based on the RPI model, which depends on three heat fluxes.

$$q_w = f(q_{conv}, q_{evap}, q_{quench}) \tag{2.47}$$

Where q_{conv} is the convective heat flux, q_{evap} is the heat flux from evaporation and q_{quench} is the heat flux from quenching.

2.2.6.1 Convective heat flux (q_{conv})

Convective heat flux consists of the forced convective heat flux contributions of both phases. The convective heat flux is based on the mixture of the two phases. The subcooled boiling model assumes full liquid contact with the superheated wall, but as the temperature increases, more surface will be covered by vapor, known as the Dry-out area.

2.2.6.2 Evaporative heat flux (q_{evap})

Evaporative heat flux describes the heat flux due to the evaporation of liquid close to the wall. It models the heat flux dependent on the nucleation site density. Equation 2.48 describes the evaporation heat flux. The evaporation heat flux also depends on the bubble diameter, bubble departure frequency, vapor density and latent heat of vaporization.

$$q_{evap} = Nf\left(\frac{\pi d_d^3}{6}\right)\rho_g h_{lv} \tag{2.48}$$

From this equation, the evaporative mass can be evaluated for the bulk boiling model, as shown in equation 2.49. This becomes the source term for the rate of interphase mass transfer.

$$\dot{m}''_{evap} = \frac{q_{evap}}{h_{lv}} \tag{2.49}$$

2.2.6.3 Quenching heat flux (q_{quench})

Bubble induced quenching occurs when the subcooled fluid enters the wake formed below a departing bubble. The quenching contributes to a higher heat flux since the bulk liquid, with a lower temperature, quenches the superheated region. This component was defined by Del Valle and Kelling [29]. The quenching heat flux is defined as shown in equation 2.50.

$$q_{quench} = h_{quench} s_{quench}(T_w - T_l) \tag{2.50}$$

Where s_{quench} is a correction factor defined as:

$$s_{quench} = \frac{T_w - T_{quench}}{T_w - T_l} \tag{2.51}$$

The quenching heat transfer coefficient is defined as imposed by Del Valle and Kelling:

$$h_{quench} = 2K_{quench} f\sqrt{\frac{\rho_l c_l k_l t_w}{\pi}} \tag{2.52}$$

Where f is the bubble departure frequency and t_w is the time between bubble departure and the nucleation of the next bubble. Equation 2.53 defines t_w, where C_w is the wait coefficient which was proposed by Kurul and Podowski [5] as 0.8.

$$t_w = \frac{C_w}{f'} \tag{2.53}$$

K_{quench} is the effective area at which the liquid acts under the bubble as it departs. K_{quench} follows Kurul's and Podowski's definition in equation 2.54, with F_A being the area coefficient for scaling between the nucleation site area density and the wall area fraction that the bubble-induced quenching influences:

$$K_{quench} = F_A \frac{\pi d_d^2}{4} N \tag{2.54}$$

a value of $F_A = 2.0$ was set by Bartolomei and Chanturiya [30] from their 45 bar test case experiments.

2.2.6.4 Bubble Departure Frequency

The bubble departure frequency is determined using the widely used model, introduced by Cole [31]. It determines the frequency by using the bubble rise velocity as the velocity scale and bubble diameter as the length scale.

$$f = \sqrt{\frac{4}{3}\frac{g(\rho_l - \rho_g)}{d_d \rho_l}} \tag{2.55}$$

2.2.6.5 Nucleation Site Number Density

Star-CCM+ uses a modified version of the Lemmert Chawla (LC) model [32], which evaluates the active nucleation site number density. The LC model is a correlation between the wall superheat, ΔT_{sat}, and the nucleation site number density. ΔT_{sat} is calculated as:

$$\Delta T_{sat} = \min\left(\max\left(T_w - T_{sat}, 0\right), \Delta T_{max}\right) \tag{2.56}$$

Where ΔT_{max} is the maximum allowed superheat applied in the model. This limit was set for initial convergence but must be ensured not to interfere with the final solution. This is then implemented into the Star-CCM+'s modified Lemmert Chawla [33] model, which modifies the calibration constants of the original model.

$$\frac{N}{N_0} = \left(\frac{\Delta T_{sat}}{\Delta T_0}\right)^{A+B(\Delta T/\Delta T_0)} \tag{2.57}$$

Where A and B are both calibration constants and the ΔT_0 and N_0 are the reference wall superheat and the reference nucleation site density, respectively.

Wall Dryout Area Fraction

The vapor contribution is evaluated from the wall dry-out area fraction derived by Weisman and Pei [34], K_{dry}, which estimates the relative contribution of the liquid and vapor phases to the convective and boiling heat transfer rates. The model uses a basic break-point; i.e. when the vapor fraction exceeds a certain threshold, only vapor convection contributes to the wall heat flux.

$$q_w = q_{conv} + (q_{evap} + q_{quench})(1 - K_{dry}) \tag{2.58}$$

K_{dry} is defined as the bubbly layer volume fraction, α_δ exceeds the required wall-dryout break-point, α_{dry}, set by the user. The bubbly layer volume fraction is defined as the average over a layer thickness δ, using the wall-normal derivative of the volume fraction.

$$\alpha_\delta = \frac{1}{\delta}\int_0^\delta \left\{\alpha_g(y_c) + \alpha_g'(y_c)(y - y_c)\right\} dy = \alpha_g(y_c) + \alpha_g'(y_c)\left(\frac{\delta}{2} - y_c\right) \tag{2.59}$$

K_{dry} can then be defined as:

$$K_{dry} = \begin{cases} 0, & \alpha_\delta \leq \alpha_{dry} \\ f(\beta), & \alpha_\delta \geq \alpha_{dry} \end{cases} \tag{2.60}$$

Where the function $f(\beta)$ is defined as:

$$f(\beta) = \frac{\alpha_\delta - \alpha_{dry}}{1 - \alpha_{dry}} \quad : \quad \alpha_{dry} \leq \alpha_\delta \leq 1 \tag{2.61}$$

Weisman and Pei noted that the maximum vapor volume fraction was 0.82 for a bubbly layer of 5.5 times the bubble departure diameter.

2.2.7 Table of Selected Models

Table 2.1 shows a summary of the models used for the study.

Table 2.1: Reference boiling models used in the study

Models	Sub-Models	Equations
BBM	Forced Convection (FCHT) [2.4]	$q_{fc} = h_{fc}(T_w - T_b)$
	Rohsenow (FDB) [2.2]	$q_{FDB} = \mu_l h_{lv} \sqrt{\frac{g(\rho_l - \rho_v)}{\sigma}} \left(\frac{c_l \Delta T_{sat}}{C_{sf} h_{lv} Pr_l^{n_p}} \right)^m$
	Boiling Departure Lift-off (BDL) [2.3]	$q_{BDL} = q_{fc} + q_{nb} \cdot S_{flow} S_{Sub}$
	Blended Boiling Model (BBM) [2.30]	$q_{BBM} = (1 - \Pi_{int}) \cdot q_{BDL} + \Pi_{int} \cdot q_{FDB}$
DBBM	Dry Heat Transfer [2.38]	$q_{dry} = \frac{Nu_g \cdot k_g}{L} (T_w - T_g)$
	Dry-spot Blended Boiling Model (DBBM) [2.37]	$q_{DBBM} = [(1 - \Pi_{int}) q_{BDL} + \Pi_{int} q_{FDB}] (1 - \Pi_{dry}) + q_{dry} \Pi_{dry}$
RPI	Kurul & Podowski (RPI) [2.58]	$q = q_{conv} + q_{quench} + q_{evap}$
	Forced Convection	$q_{conv} = h(T_w - T_f)$
	Quenching	$q_{quench} = h_{quench} s_{quench} (T_w - T_l)$
	Evaporation	$q_{evap} = N f \left(\frac{\pi d_d^3}{6} \right) \rho_g h_{lv}$

3
Methodology

3.1 Academic Baseline Setup Process

The experimental setup used by Gholinia et al. [35] is modeled in STAR-CCM+ to validate the different boiling models against experimental data and compare their predictive performance. This academic baseline case will be used for the implementation and calibration of the boiling models.

The experiment consisted of three cartridge heaters enclosed in three solid blocks, each composed of a copper bottom part, a cast-iron top, and a small composite insulator around the top part. These blocks were inserted into the Plexiglas channel and their top surface is in contact with a liquid coolant flowing through the channel, as shown in Figure 3.1.

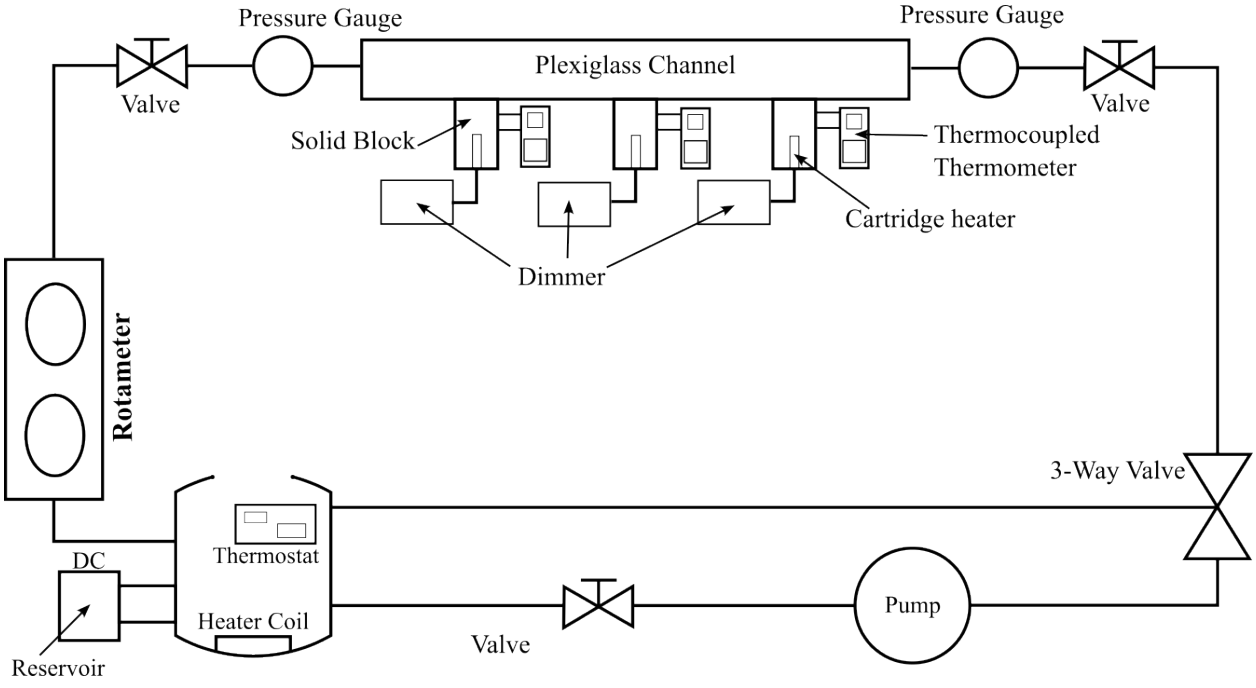

Figure 3.1: Experimental Setup Schematic [35]

The variable velocity pump, together with the bypass valves, was used to set the required pressure and velocity of the liquid coolant, while the heater coil warms up the bulk liquid. The cartridge heaters are connected to dimmers to vary the total heating power into the system with the intention to represent thermal loads

from combustion cycles. In this case, the dimmer modules are assumed to equally distribute the heating power to all three contact surfaces on the interior of the copper bottom-part, as seen in Figure 3.2

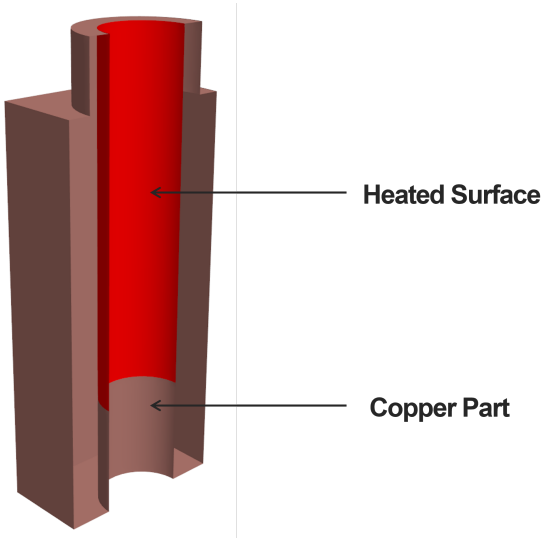

Figure 3.2: Location of Heated Surface on the Copper-part, where the heating Cartridge introduces heat into the system.

The heat flux for a given cartridge heater is therefore $Power/(3\pi DL)$ $[W/m^2]$ and the wall temperature is an average value measured at 3 different locations. In the experiment, the wall temperature was extrapolated from temperatures measured at two points along the direction of nominal heat flow, below the surface of the sample in contact with the liquid. In STAR-CCM+, the wall temperature is directly obtained at the surface of the wall in contact with the liquid.

Table 3.1: Academic Baseline Setup

Parameter:		**Value:**
Duct Width	$[mm]$	30
Duct Height	$[mm]$	20
Hydraulic Diameter	$[mm]$	24
System Pressure	$[bar]$	1.2 - 1.5
Velocity Inlet	$[m/s]$	0.46 - 0.77 - 1.23
Temperature Inlet	[°C]	90 - 101.89
Coolant Composition	[-]	50/50 EG/W

The channel dimensions of operating conditions are shown in Table 3.1. for more details. A cross-sectional view and an isometric view of the test section are shown in Figure 3.3 and 3.4, respectively, where the materials are color-coded.

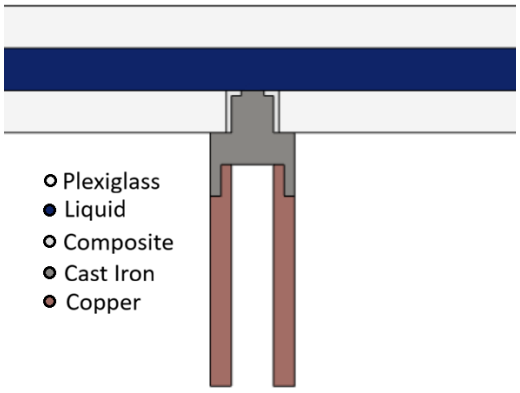

Figure 3.3: Cross-Section View

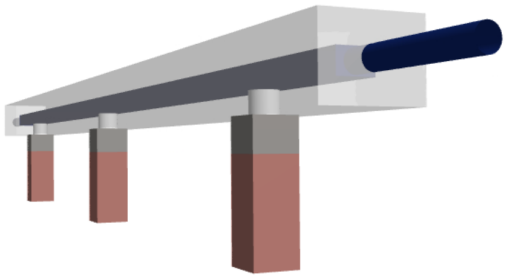

Figure 3.4: Isometric View

3.1.1 Forced Convective heat-flux

The convective heat transfer is modeled such that it is possible to estimate the wall temperatures for heat fluxes Q in the range 0 to $50kW/m^2$, which is the whole span of available experimental data. A CFD-CHT model of the test section is set up in STAR-CCM+, see Table 3.2 for the general settings used in all models. With this setup, the contact resistance on the outside wall is adjusted for ambient air.

Table 3.2: FCHT - Settings

Solver settings:
Steady State
Realizable K-Epsilon Two-Layer Solver
Two-Layer All y+ Wall Treatment
Polynomial Density
Segregated Flow

3.1.2 Single-phase Rohsenow Model

Experimentally, the relationship between applied heat flux and wall temperature exhibits two distinct regimes: an initial linear regime corresponding to single-phase convection, followed by a nonlinear regime where the wall temperature increases slightly while the heat flux increases significantly. This behavior is associated with the onset of nucleate boiling at the onset temperature (T_{ONB}), where heat transfer is significantly enhanced.

In STAR-CCM+, the use of a single-phase model to represent boiling does not account for the vaporization of the liquid and, thereby, the presence of a vapor phase. Instead, the boiling effects are incorporated through an empirical correlation in this case the Rohsenow Correlation. This will enhance wall heat transfer without resolving bubble dynamics. The model is dependent on vapor density, surface tension from the liquid and the latent heat, calculated according to Equation 2.42, which is

a balance of the saturation enthalpies of the two phases. The values used are shown in Table 3.3.

Table 3.3: Rohsenow Parameters

Parameter:		**Value:**
Latent Heat	$[J/kg]$	2 256 765
Vapor Density	$[kg/m^3]$	1.5473
Surface Tension	$[N/m]$	0.05268759
C_{sf}	[-]	0.012
n_p	[-]	1.25

3.1.3 RPI model

As mentioned previously, the Heat-Transfer Based Boiling/Condensation model is already implemented in Star-CCM+ (Version 2602) Mixture Multiphase solver using the aforementioned physical representation of evaporative and quenching heat fluxes. Implementing and fitting the coefficients to match the experimental data points provided by Gholinia et al. [35], this also helps adjust the solver settings in a simplified environment.
In addition to the already selected models in FCHT; the selected models are:

Table 3.4: Chosen models for Heat-Transfer Based Boiling model

Solver settings:
Mixture Multiphase
Gradients
Multiphase Interactions
Segregated Multiphase Temperature
Gravity

And further models are chosen within the Multiphase Interaction node for the wall and bulk boiling models:

Table 3.5: Chosen models for multiphase interactions

Multiphase Interaction:
Heat-Transfer Based Boiling/Condensation
Slip Velocity
Wall Nucleate Boiling
Wall Bubble Nucleation
Wall Transient Conduction (Quenching)

3.1.3.1 RPI model Properties

In order to get the best fit with the experiments, certain parameters need to be adjusted to fit the case of cast-iron in combination with the ethylene glycol-water

mixture. Different properties were tested during the baseline validation to match the experiments conducted by Gholinia et al. [35].

In Star-CCM+, the Lemmert Chawla (LC) model is used as the default model for nucleation site density. The boiling heat flux was highly sensitive to LC model parameters and were directly proportional to the extent of boiling occurring in the system. The superheat limit ΔT_{max} was increased to $60K$, to avoid interference with the final solution.

Evaluation of different sub-models of bubble departure diameter was undertaken to calibrate the model. The default model was tested, consisting of correlations of superheat temperatures by Tolubinsky-Kostanchuk [36]. Many CFD solvers implement these models because of their simplicity. Mazzocco [18] also stated that the empirically correlated models that CFD solvers often use do not account for local fluctuations in flow quantities and are calculated using bulk flow quantities. Therefore, the bubble departure diameter derived from the theory of bubble force balance 2.2.2.1 models was also evaluated. This helped in comparing with the BBM and with ways of changing the growth constant of the bubbles when introducing the parameter b.

The parameters of sub models, Dry-spot and wall transient conduction, were kept at the recommended values set by Weisman and Pei [34] and Del Valle and Kelling [29].

Table 3.6: RPI Boiling Parameters

RPI Parameters:	
b	0.2
N_{ref}	8000
$A(LC)$	1.805
$B(LC)$	0
ΔT_{max}	60 K
K_{quench} (wall area fraction)	2.0 (Kurul)
C_w	0.8 (Del Valle)

3.1.3.2 Mesh dependencies & limitations

During the initial evaluations, the solver showed signs of numerical indicated by a high volume fraction at the wall-adjacent cell. To overcome this issue, the height of the first cell in the boundary layer must be sufficiently large enough to ensure that the vapor volume generated at the wall does not exceed the volume of the cell. To mitigate these instabilities, a sufficiently large boundary layer cell thickness and a low boundary layer cell count were implemented. This would consecutively lower the volume fraction at the wall cell.

3.1.4 Blended Boiling Model

The Blended Boiling Model is implemented into StarCCM+ as a custom library which is programmed and compiled with the programming language C. Macros were developed to automate the initial setup of the model explained in Chapters 2.2.2, 2.2.1 and 2.2.3.

The C-program script consists of functions that calculate: nucleate boiling heat transfer coefficients, temperature at the onset of nucleate boiling, bubble departure radius, flow induced suppression of nucleate boiling, fully developed nucleate boiling, nucleation site density and probability of bubble interaction. This is then compiled into a library that is read into STAR-CCM+, using the *User Code* functionality.

Java-macros define general field functions for thermophysical properties, saturated properties, linearized coefficients and q_{boil}. It also creates field functions and user expressions in STAR-CCM+ that are used to tune the BBM. The macros also generates field functions necessary for the mixture multiphase framework and derivation of the mixture multiphase sources from first principles, following the theory explained in Chapter 2.2.5.

For additional stability, the boiling heat flux term q_{boil}, defined in Eq. 2.30, can be under-relaxed (q_{UR}) following the implementation guidelines provided in the Simcenter STAR-CCM+ knowledge base [37].

Finally, it creates the heat transfer coefficients that are used on the relevant fluid contact surface. In STAR-CCM+, the function *User Defined Wall Heat Flux Specification* can be coupled with field functions to express any additional heat flux on relevant contact surface boundaries. This is done by modifying the coefficients (A, B, C and D) from the linearized expression for the wall heat flux.

$$q_w = A + BT_c + CT_w + DT_w \tag{3.1}$$

Where, T_c and T_w are the temperature in the cell closest to the wall, and the wall-cell temperature, respectively. The coefficients are defined as a summation with the user defined part and an internally computed part as in Eq. 3.2.

$$\begin{aligned} A &= A_{user} + A_{internal} \\ B &= B_{user} + B_{internal} \\ C &= C_{user} + C_{internal} \\ D &= D_{user} + D_{internal} \end{aligned} \tag{3.2}$$

Where the definitions of the user defined coefficient are shown in Appendix A. This creates a user-specified wall heat flux on relevant contact interface boundaries to remove heat due to nucleate boiling as calculated in Equation 2.30. Further, the empirical parameters are set as seen in Table 3.7.

Table 3.7: Baseline BBM parameters

Parameter:	Value:	Source:
b	0.2	Zuber [20], Eq. 2.14
C_s	20/3	Zeng et al. [19], Eq. 2.13
C_{sf}	0.01	Rohsenow [12], Eq. 2.2
m	3.0	Eq. 2.2
n_p	1.0	Eq. 2.2
N_0	1000	Li et al. [25], Eq. 2.34
ϕ_0	60	Eq. 2.36

3.1.5 Boundary Conditions

The experiments were performed for a number of inlet velocities, system pressures, and bulk liquid temperatures. To validate the simulations, three different cases were selected to capture a wide range of different operating conditions, as shown in Table 3.8.

Table 3.8: Baseline Boundary Conditions

Case:	A: Velocity Inlet	B: System Pressure	C: Temperature Inlet
1	0.77 m/s	1.2 bar	101.89 ℃
2	1.23 m/s	1.5 bar	90 ℃
3	0.46 m/s	1.5 bar	90 ℃

For the heat flux, the experiments include fixed values at: 0, 4, 8.4, 12.5, 16.5, 20.5, 24, 28, 32, 36, 40 and 44.5 kW/m^2. In the simulations, a sweep was carried out over 0, 10, 20, 30, 40 and 50 kW/m^2. No contact resistances were assumed between the different solid parts. A convective boundary condition was specified on the outside wall with the ambient temperature of $300K$ and a Heat transfer coefficient of 3.5 W/m^2, adjusted to simulate the heat transfer from the environment from the tests.

3.1.6 Mesh Settings for Baseline Setup

The computational domain was discretized into polyhedral control volumes, with additional mesh refinement near the interface between the liquid coolant and the surrounding solid structures. This refinement improves the accuracy of the high near-wall gradient of velocity and temperature at the heated wall. Figure 3.5 and 3.6 shows both the cross-sectional view of the mesh and in the vicinity of the heated surface.

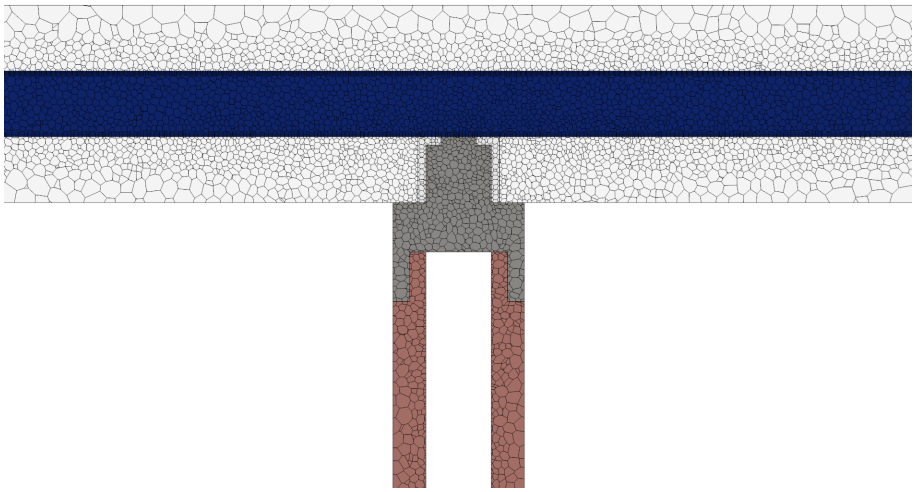

Figure 3.5: Mesh Cross-Section View

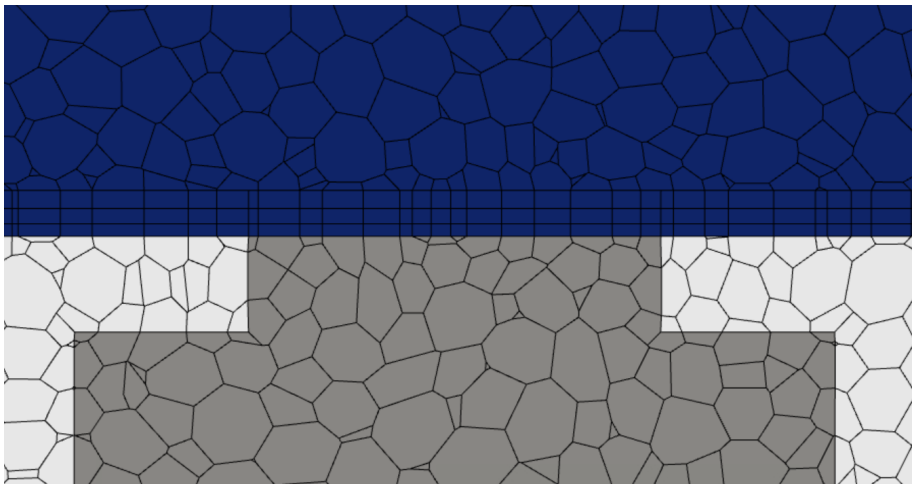

Figure 3.6: Detailed Cross-Section View in the vicinity of the heated surface (Grey)

It is of great importance to consider the height of the near-wall cell. In Vasudevan's et al [38] study, it was observed that with an average wall $y^+ = 1.8$, the wall heat flux was over-predicted. The study further investigated that for a refined near-wall cell, the diameter of the vapor bubble is larger than the height of the near-wall cell. The study also showed that for a wall $y^+ = 14$ yielded accurate results. Therefore, this was established as a guideline for the Wall y^+, and a cell thickness of the first cell was set to 1.2 mm, for the baseline setup. In Table 3.10 mesh parameters used in the simulations are listed.

Table 3.9: Mesh Settings

Parameter:		**Value:**
Mesh Type	[-]	Polyhedral
Base Size	[mm]	8
Number of Cells	[#]	1 176 613
Number of Boundary Layers	[#]	3

3.2 Thermophysical Properties

The liquid coolant used in automotive applications is a mixture of water and ethylene glycol. Ethylene glycol reduces the freezing point of the mixture and, hence, acts as an antifreeze. In this study, two different coolant mixtures have been considered: a 50% volume mixture for the baseline setup and a 40% volume mixture for the engine setup, consisting of ethylene glycol ($C_2H_6O_2$) and water (H_2O), respectively. This ensures the ability to closely replicate the experimental conditions. This will potentially minimize the uncertainty of the influence of thermophysical properties in the coolant.

At the boiling point of the mixture, the vapor generated is assumed to be only water vapor, since the saturation temperature of water is lower than the boiling point of ethylene glycol. Temperature dependent thermophysical properties of the liquid coolant and cast-iron obtained from Volvo's internal material databases are used.

3.3 Engine CFD-CHT Simulation Setup

Two different variants of an in-line, 13 liter, 6 cylinder heavy-duty engine were considered. For both of these variants, the liquid coolant circulates through the cylinder block and cylinder head to reduce the material temperature to acceptable levels during combustion. Figure 3.7 shows a schematic of the cooling system.

The coolant in the cooling system is circulated by the pump inlet and first flows to the coolant duct cover and oil cooler, then to the engine block region surrounding the cylinder liners. As it passes along the liner walls, the coolant absorbs heat from the walls of the combustion chamber and its temperature increases. A portion of the heated coolant exits the EGR (Exhaust Gas Recirculation) cooler before entering the cylinder head, while the coolant is introduced into the cylinder head region. Within the cylinder head, the coolant flows through dedicated cooling channels that remove heat from high-temperature regions. Finally, the coolant exits the engine through the thermostat outlet and, depending on the operating conditions, flows to the radiator, where it is cooled before being recirculated back to the pump.

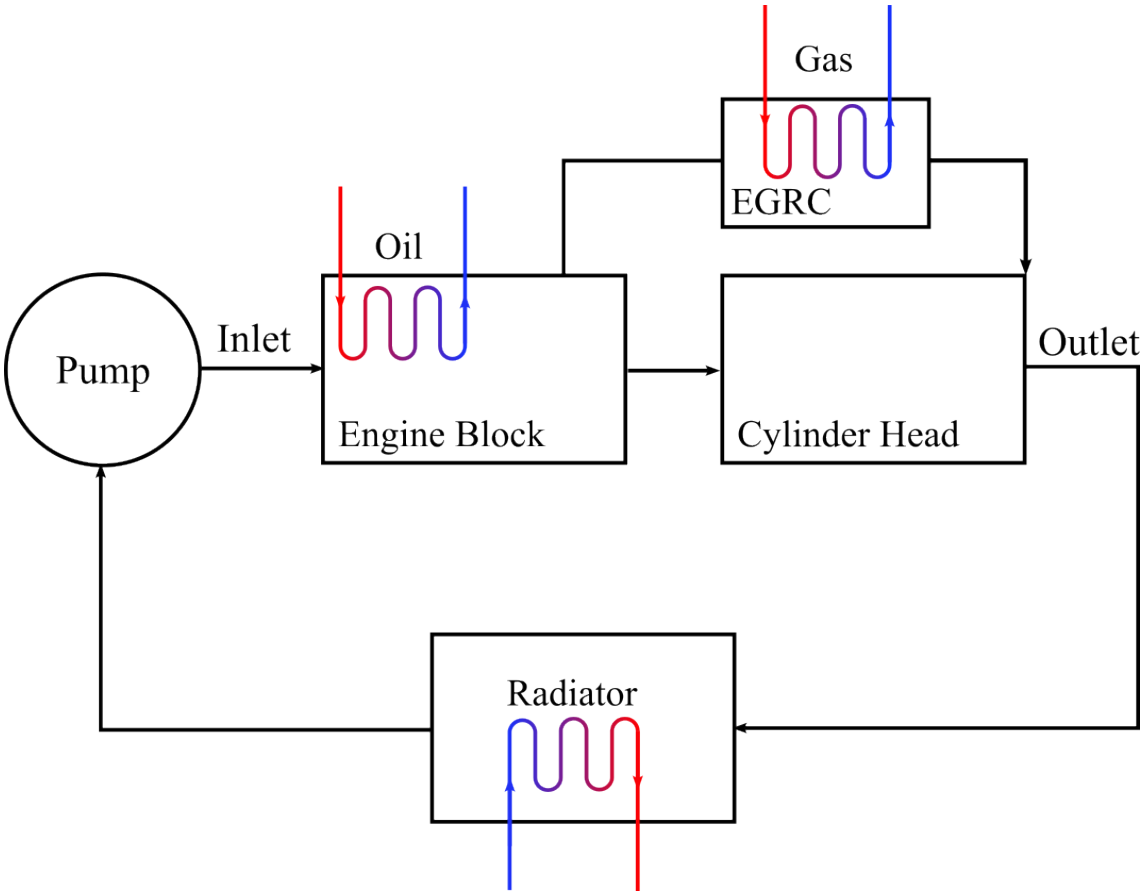

Figure 3.7: Engine Geometry - Containing: Fluid Cylinder head, Fluid Cylinder Block, Block and Solids

Using experiments conducted on engine models 1 and 2, a comparative analysis of the models can be performed for validation. The experiments, consisting of fixed mass flow rate with varying pressure and vice versa, will be analyzed for relative influence under the different conditions for engine 1. The temperature of the cylinder block and cylinder head is measured in different positions using thermocouples in the experiments. The nominal positions of these thermocouples were replicated using point probes in the CFD-CHT simulation model for comparison of the simulation results with those from the experiments. The simulation wall boundaries consist of the combustion and the ambient, respectively.

3.3.1 Boundary Conditions

In STAR-CCM+ the boundary conditions for both Engine models 1 and 2 are as follows:

Fluid Cylinder Block:

- Mass Flow Inlet - for the pump inlet
- Mass Flow Outlet - for the EGR outlet

Fluid Cylinder head:

- Mass Flow Inlet - for the EGR return
- Pressure Outlet - for the thermostat outlet

Solids:

- Convective boundary conditions are prescribed from *Converge CFD* combustion simulations onto combustion cylinders 1 to 6 - on the combustion chamber intake/exhaust ports, valves, valve seats and valve guides.

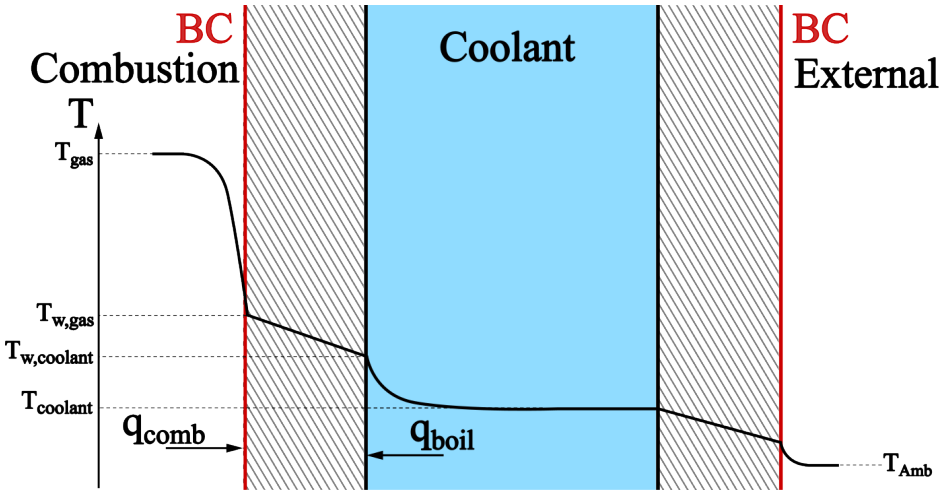

Figure 3.8: Representation of boundaries with temperature

The boundary conditions for the fluid cylinder head and block for all cases were attained internally through Volvo's experiments on the engine models 1 and 2. These cases were termed N1 and N2, for the nominal cases of engine 1 and 2, respectively. The case with varying pressure included 9 different experiments, where the pressure gradually decrease from P1, The highest pressure to P9, the lowest pressure for engine model 1. For cases with varying mass flow, the mass flow was increased from M1 (the highest mass flow rate) to M7 (the lowest mass flow rate).

The measurement probes are denoted by names representing cylinder numbering, radial position from the center and angles in polar coordinates. A visual representation of the probes around a cylinder is shown in Figure 3.9, where the starting number, which for the illustrated example is 4, represents cylinder number four, and the latter numbers from 0-2 are the radial position from the center. Lastly the angular position are denoted W (West), N (North), E (East) and S (South), respectively. These measurement probes are used to measure the temperatures and was defined to be able to make comparisons with the experimental test rig setup.

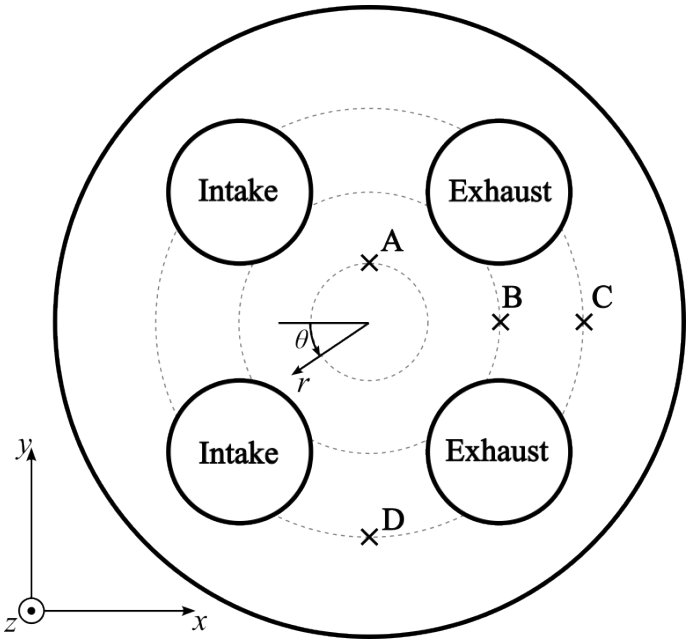

Figure 3.9: Illustration of Probe Positioning examples for Cylinder 4: A) 4N0, B) 4E1, C) 4E2, D) 4S2

3.3.2 Mesh Settings for Engine Setup

Similar base settings were used for the engine, based on the academic baseline setup, but smaller cell sizes are necessary to accurately solve the complex flow dynamics of the engine coolant jacket. As explained in chapter 3.1.6, the near wall cell needs a wall y^+ of roughly 14, to yield accurate results and not over-predict the boiling heat flux. Therefore, the base size of the cells was kept minimal, but the boundary layer cell thickness was set to 1.2 mm, to satisfy the wall y^+ criterion. Table 3.10 shows the settings used for the engine case.

Table 3.10: Engine Mesh Settings

Parameter:		**Value:**
Mesh Type	[-]	Polyhedral
Base Size	[mm]	4
Number of Cells	[#]	53 349 485
Number of Boundary Layers	[#]	2
Boundary Layers Thickness	[mm]	1.2

3.3.3 Baseline Tuning & Additional Tuning

Previously explained models for the baseline setup process in Chapters 3.1.1, 3.1.2, 3.1.3 and 3.1.4 were implemented. This includes Forced Convection Heat Transfer (FCHT) model, Single-phase Rohsenow (SP) model, Heat Transfer Based Boiling (RPI) model and Blended Boiling Model (BBM).

Additional tuning was performed for both RPI and BBM to improve prediction accuracy. The logic behind this is that the models parameters are sensitive to material-fluid combinations. In particular, the coolant composition differs between the cases, i.e. the baseline and the engine setup; with ethylene glycol-water volume mixtures of 40% and 50%, respectively. Furthermore, uncertainties in the surface roughness of the cast-iron, such as the degree of polishing, may influence the results by altering the effective material-fluid interaction.

Comparisons between the models in the engine case will be presented with the baseline tuning and the additional tuning in Chapter 4.2.2.

Table 3.11: BBM parameters for Engine setup

	Baseline Tuning	**Additional Tuning**
b	0.2	-
C_s	20/3	-
C_{sf}	0.01	0.005
m	3.0	-
n	1.0	-
N_0	1e3	5e5
n_p	1.0	-
ϕ_0	60	-

Additional tuning was also needed for the RPI model to better match the increased superheated temperatures of the simulation and the new solid-fluid combination.

Table 3.12: RPI parameters for Engine setup

	Baseline Tuning	**Additional Tuning**
b	0.2	-
N_{ref}	8000	30000
$A(LC)$	1.805	-
$B(LC)$	0	-
K_{quench}	2.0	-
C_w	0.8	-

3.3.4 Influence of BBM Parameters

A sweep of BBM parameters including b, C_{sf} and N_0 was made for the engine case setup to understand the potential linear and/or non-linear behavior. The three parameters were selected because they influence different components of the BBM framework. The b-parameter affects the bubble growth constant and thereby influences the BDL part. The C_{sf}-parameter governs the FDB heat flux through the Rohsenow correlation. The N_0-parameter determines the number of active nucleation sites and thus impacts the calculation of the prediction/blending factor Π.

3.3.5 Risk of Film Boiling

The experimental data available for Cylinder 4 (see Figure 3.10) will be used to further investigate the risk of film boiling.

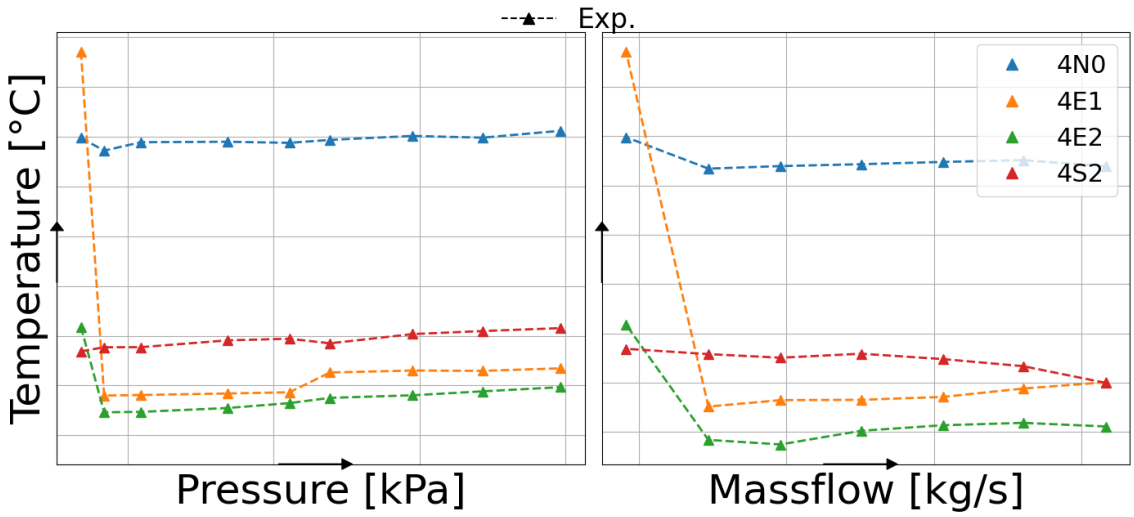

Figure 3.10: Experimental Values for Probes in Cylinder 4

This is done by creating spherical observation regions around the virtual temperature probes in cylinder 4 and adjacent probes in cylinders 1 to 6 to estimate the probabilities (Π_{int} and Π_{dry}). Due to the uneven surface of the cooling jacket, different radii will be used for the spheres to keep the area in contact with the fluid region constant. See Table 3.13.

Table 3.13: Equivalent sphere radius and threshold surface area for selected probes around Cylinder 4, and at exhaust-exhaust Bridge.

Probe	**Radius of Sphere [mm]**	**Surface Area [mm^2]**
Around Cylinder 4:		
4N0	13.30	47.765
4E1	6.10	48.773
4E2	6.80	48.607
4S2	7.99	46.136
Exhaust-Exhaust Bridge:		
1E1	6.10	49.105
2E1	6.10	48.165
3E1	6.10	49.497
4E1	6.10	48.773
5E1	6.10	48.160
6E1	6.10	48.820

These spherical observation regions are illustrated in Figures 3.11 and 3.12.

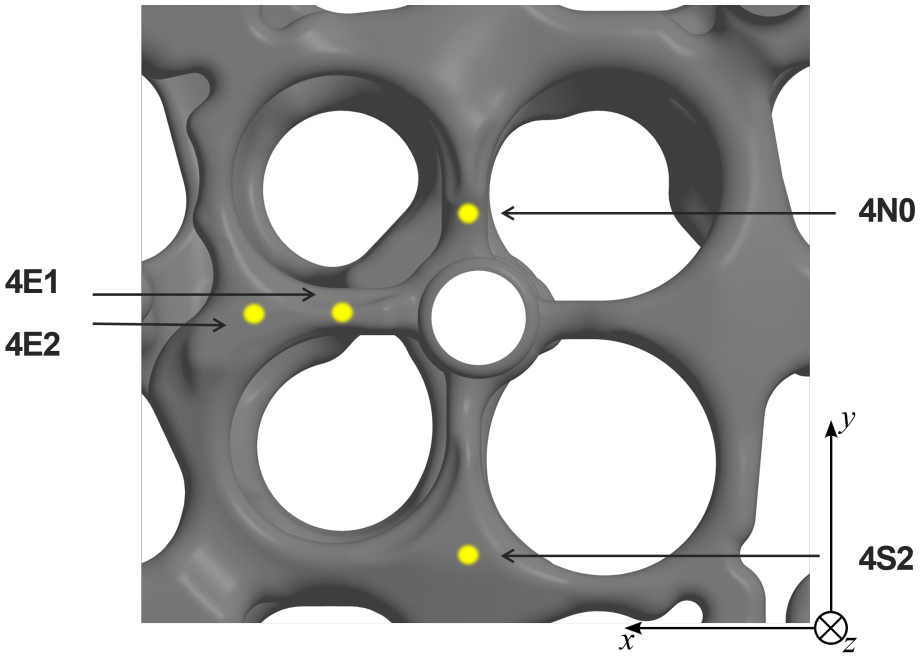

Figure 3.11: Illustration of Spherical Observation Regions Around Cylinder 4

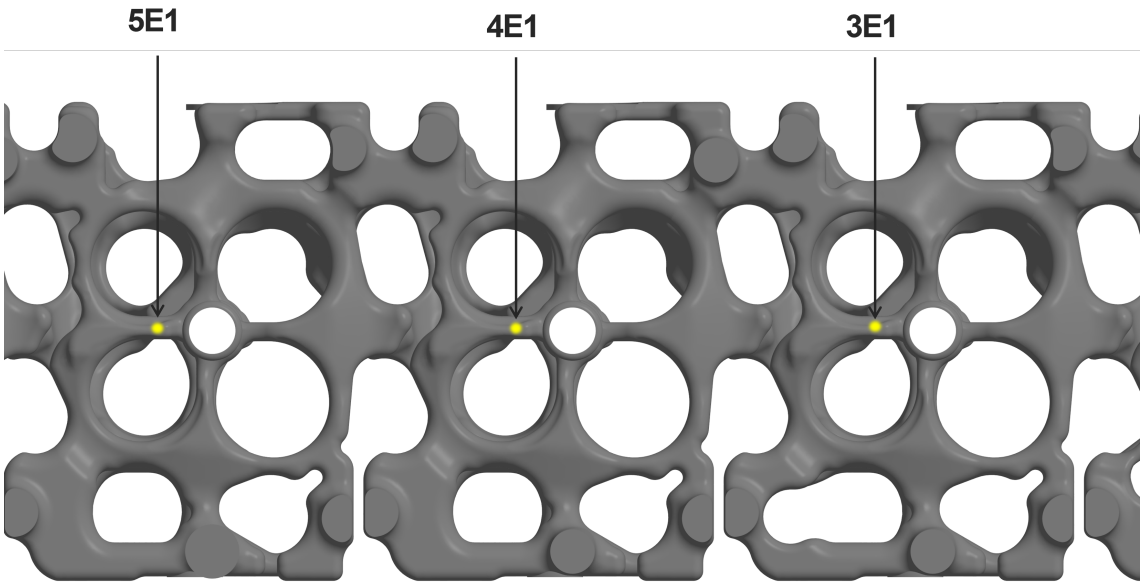

Figure 3.12: Illustration of Spherical Observation Regions in Cylinder 5, 4 and 3 at exhaust-exhaust bridge

3.3.6 Probability of Dry-spot (Π_{dry})

The additional custom probability (Π_{dry}) is used to blend the two heat fluxes, q_{BBM} and q_{dry} in Eq. 2.38 and is defined as the probability of 5 or more surrounding bubbles. This will effectively simulate dry-spots in the model where temperatures are expected to increase significantly. Further calibration was needed to match the results with the new model. The settings used for the DBBM is seen in Table 3.14.

Table 3.14: BBM parameters for Engine setup

	BBM parameters	**DBBM parameters**
b	0.2	-
C_s	20/3	-
C_{sf}	0.005	-
m	3.0	-
n	1.0	-
N_0	5e3	6e3
n_p	1.0	-
ϕ_0	60	-

4

Results

4.1 Academic Baseline Test Case

The following results are for the academic baseline setup case, including FCHT and Rohsenow correlation comparisons against experimental values for all 3 baseline cases, as seen in Table 3.8. Variants of the RPI model against experimental values and variants of the BBM against experimental values are included as well for all baseline cases. This is to calibrate the models and investigate the influence of different operating parameters. A selection from these models, investigated in the academic baseline case, are chosen for the engine CFD-CHT simulation.

4.1.1 FCHT & Rohsenow Correlations

Comparisons between FCHT (no boiling), Single-phase (SP) and Multiphase (MP) Rohsenow Correlations. The operating condition for each case is provided as a tittle to each of the plots in Figure 4.1, where A, B and C are velocity inlet, system pressure and temperature inlet, respectively, as described in Table 3.8 in Chapter 3. The computed ΔT_{avg} is the average temperature difference between the predicted- and experimental temperatures.

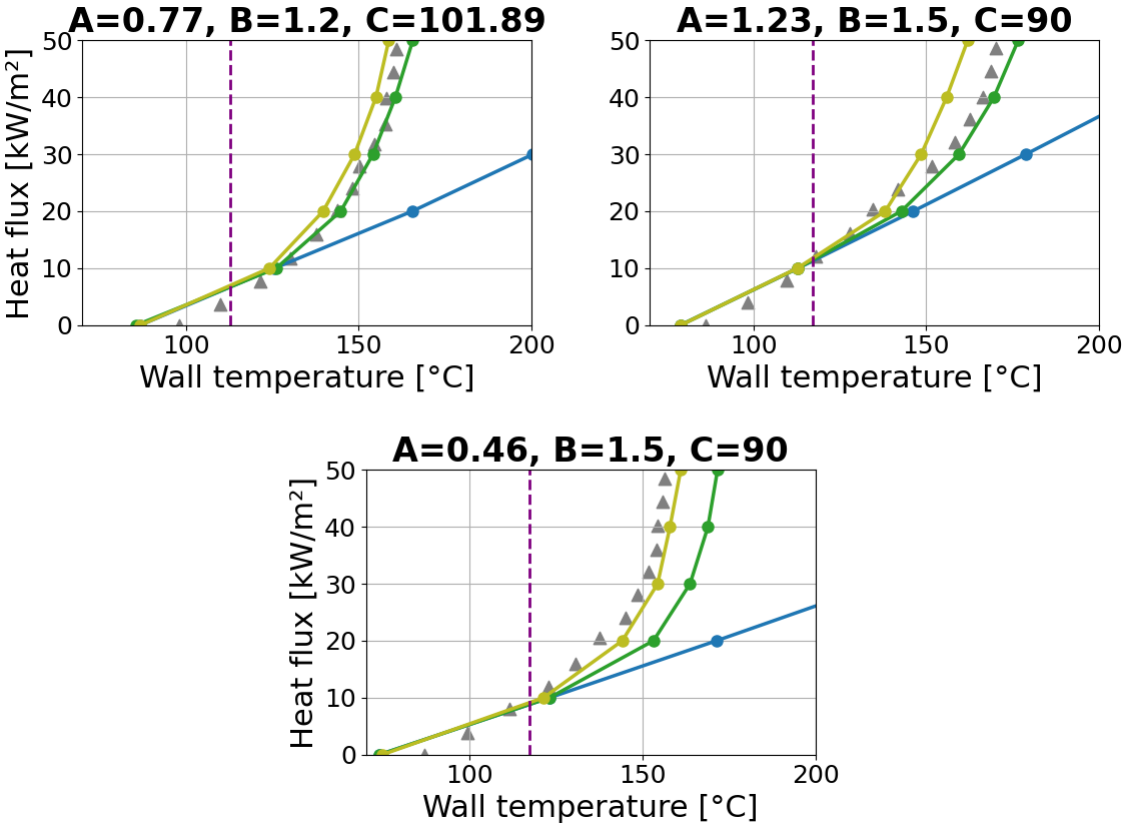

	Models:	ΔT_{avg} [$C°$]:
	FCHT (no boiling)	44.88
	Single-phase Rohsenow	7.16
	Multiphase Rohsenow	5.43
	Exp.	
	T_{sat}	

Figure 4.1: Results for FCHT & SP Rohsenow Correlation. A, B and C corresponds to velocity inlet, system pressure and temperature inlet, respectively.

4.1.2 RPI Model

Various sub models were tested while evaluating the RPI model. These sub models were used to model the nucleation site density and bubble departure diameter. A comparison of results from these different evaluated implementations of the RPI model are shown in Figure 4.2. The proposed model used the Lemmert-Chawla [32] Nucleation site number density model and the Steiner-Mazzocco for the Bubble Departure Diameter model, which mixes the Bubble growth forces from Steiner [13] and Drag and lift forces from Mazzocco [18]. These models were selected for their prediction accuracy and operational simplicity. The computed ΔT_{avg} is the average temperature difference between the predicted- and experimental temperatures.

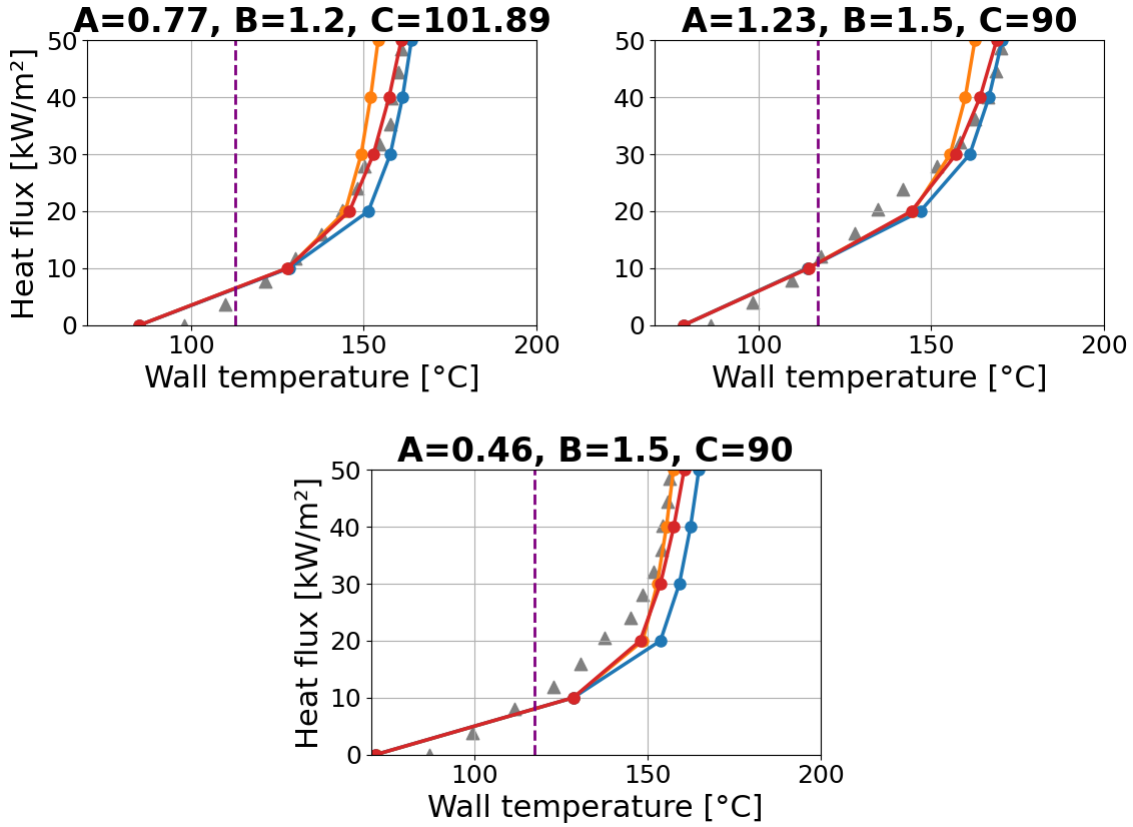

Models:	Nucleation Site Density:	Bubble Departure Diameter:	ΔT_{avg}
	Li	Mazzocco	5.99
	Li	Steiner-Mazzocco	7.07
Proposed	Lemmert-Chawla	Steiner-Mazzocco	4.99
	Exp.		
	T_{sat}		

Figure 4.2: Comparison between different implementations of the RPI model. A, B and C corresponds to velocity inlet, system pressure and temperature inlet, respectively.

4.1.3 Blended Boiling Model

Comparisons between the different Boiling Departure Lift-off (BDL) models in the Blended Boiling Model framework are presented in Figure 4.3. These different sub models present different ways of modeling the forces acting on the bubble. These include Steiner [13] and Mazzocco [18] for drag and lift forces; Zeng [19] and Rayleigh-Plesset [23] for the bubble growth force. The calculated ΔT_{avg} is the average temperature difference between predicted and experimental temperatures.

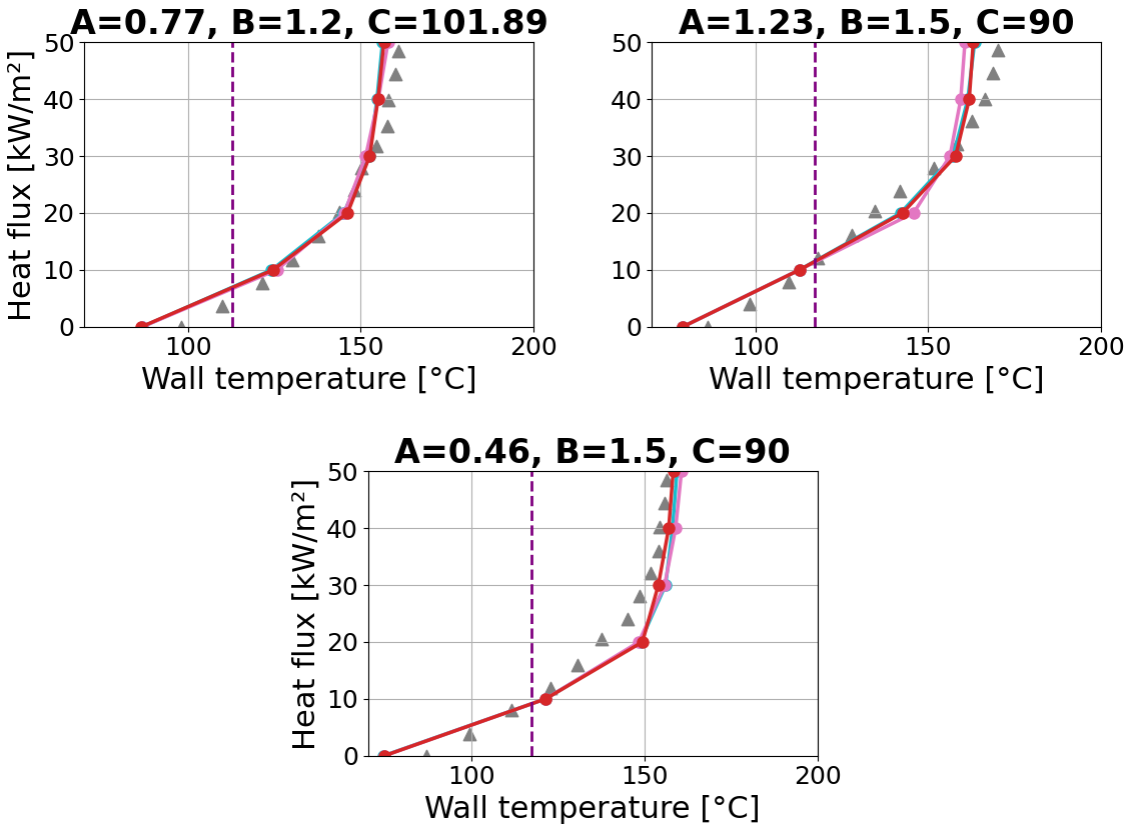

Models:	F_G	F_D	F_L	ΔT_{avg}
	Zeng	Steiner	Steiner	5.20
	Rayleigh-Plesset	Mazzocco	Mazzocco	5.57
Proposed	Zeng	Mazzocco	Mazzocco	5.06
	Exp.			
	T_{sat}			

Figure 4.3: Baseline Results for Blended Boiling Model. A, B and C corresponds to velocity inlet, system pressure and temperature inlet, respectively.

4.2 Engine CFD-CHT Simulation Results

In this section, results from the CFD-CHT simulations of a heavy-duty Volvo diesel engine are presented. The parameters of the BBM are further tuned to adapt to these cases. Therefore, these results are also compared with the model parameters that were tuned for the baseline academic case. The influence of Pressure and Mass flow rate is studied with both BBM and DBBM, and further investigation for risk of film boiling is evaluated in cylinder 4.

4.2.1 Influence of BBM Parameters

For computing average values (N_{avg}, $r_{d,avg}$, $q_{FDB,avg}$ and Π_{avg}) on the cooling jacket, a threshold of temperature values above the saturation temperature has been set to only average the values on the region of the cooling jacket where this condition is met.

4.2.1.1 Zeng's Bubble Growth Parameter - b

In this section, the influence of Zeng's bubble growth parameter in the BBM framework is evaluated in various positions in the engine. The parameter b appears in Equation 2.14. In Table 4.5 the N_{avg}, $r_{d,avg}$ and ΔT_{avg} are presented.

Table 4.1: Results of b-parameter sensitivity

		● $b = 0.02$	● $b = 0.20$	● $b = 2.00$
N_{avg}	$[sites/m^2]$	468.78 $\cdot 10^6$	69.27 $\cdot 10^6$	41.99 $\cdot 10^6$
$r_{d,avg}$	$[\mu m]$	0.609	15.41	256.35
ΔT_{avg}	$[C°]$	39.40	27.63	26.14

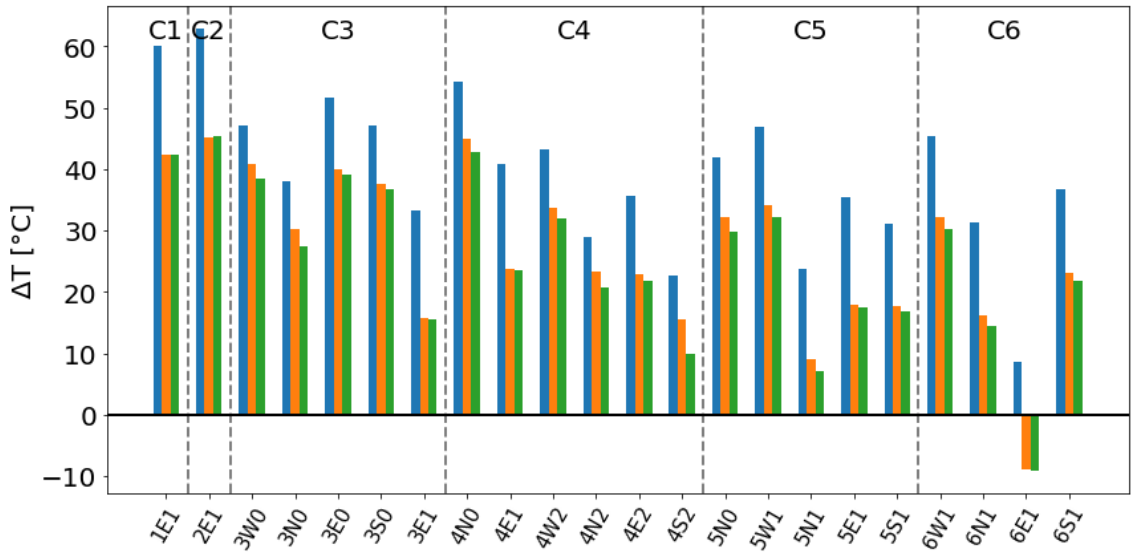

Figure 4.4: Evaluation of BBM for different values of Zeng's bubble growth parameter b

4.2.1.2 Rohsenow's Material Parameter - C_{sf}

In this section, the influence of Rohsenow's Material parameter in the BBM framework is evaluated in various positions in the engine. The parameter C_{sf} appears in Equation 2.2. In Table 4.2 the $q_{FDB,avg}$ and ΔT_{avg} are presented.

Table 4.2: Results of C_{sf}-parameter sensitivity

	$C_{sf} = 0.005$	$C_{sf} = 0.010$	$C_{sf} = 0.020$
$q_{FDB,avg}$	$-2.89 \cdot 10^5$	$-1.73 \cdot 10^5$	$-1.43 \cdot 10^5$
ΔT_{avg}	27.62	35.56	51.82

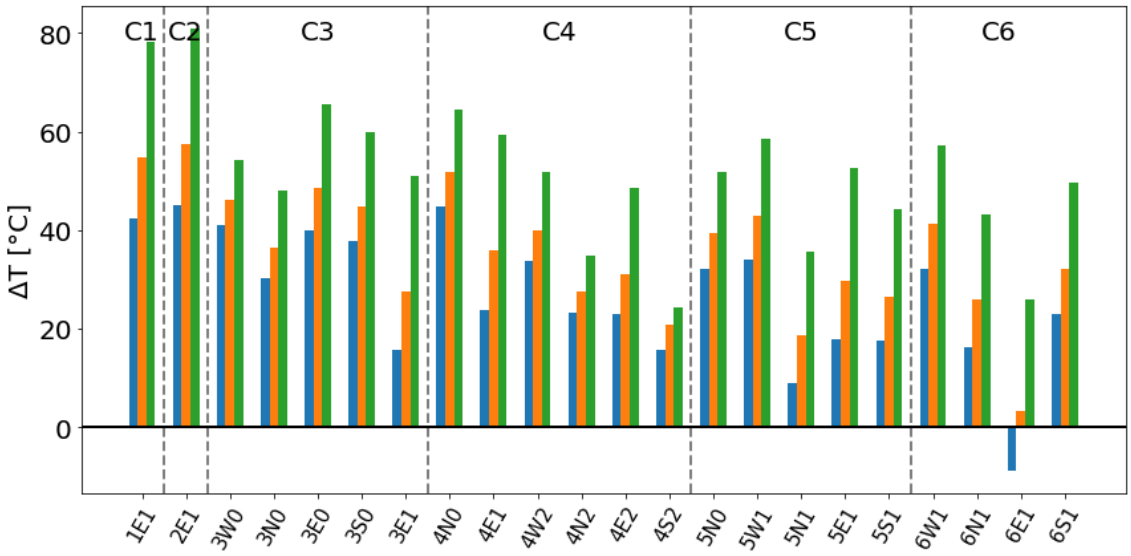

Figure 4.5: Evaluation of BBM for different values of Rohsenow's parameter C_{sf}

4.2.1.3 Li's Empirical Nucleation Site Parameter - N_0

In this section, the influence of Li's Empirical Nucleation Site Parameter in the BBM framework is evaluated in various positions in the engine. The parameter N_0 appears in Equation 2.34. In Table 4.3 the Π_{avg} and ΔT_{avg} are presented.

Table 4.3: Results of N_0-parameter sensitivity

	$N_0 = 1e3$	$N_0 = 5e5$	$N_0 = 1e8$
Π_{avg}	0.01504	0.26770	0.84752
ΔT_{avg}	32.28	27.72	26.44

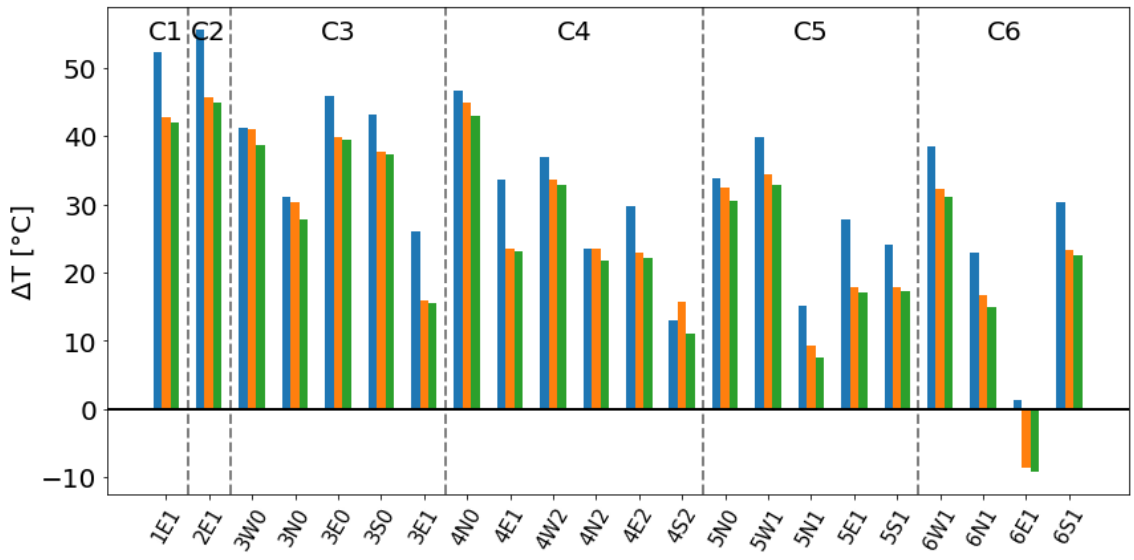

Figure 4.6: Li's Empirical Nucleation Site Parameter - N_0

4.2.2 Comparison with model parameters tuned for the baseline academic case

Results for case N1, comparing tuning parameters from the baseline setup used in the engine model and additional tuning for improved prediction capabilities. The calculated ΔT is the average temperature difference between predicted and experimental temperatures.

BBM	● **Baseline Tuning**	● **Additional Tuning**
ΔT	27.29	19.48

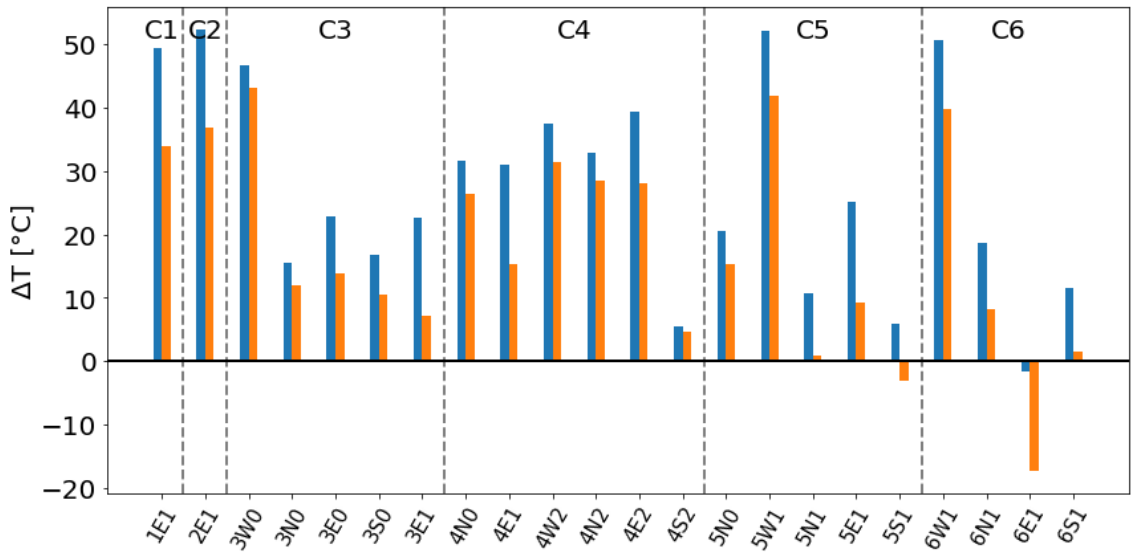

Figure 4.7: Baseline Tuning & Additional Tuning for the BBM

The RPI model was also additionally tuned for the CFD-CHT simulation of the engine. The result for N1 case in comparison is seen in Figure 4.8. The calculated ΔT is the average temperature difference between predicted and experimental temperatures.

RPI	Baseline Tuning	Additional Tuning
ΔT	30.92	21.35

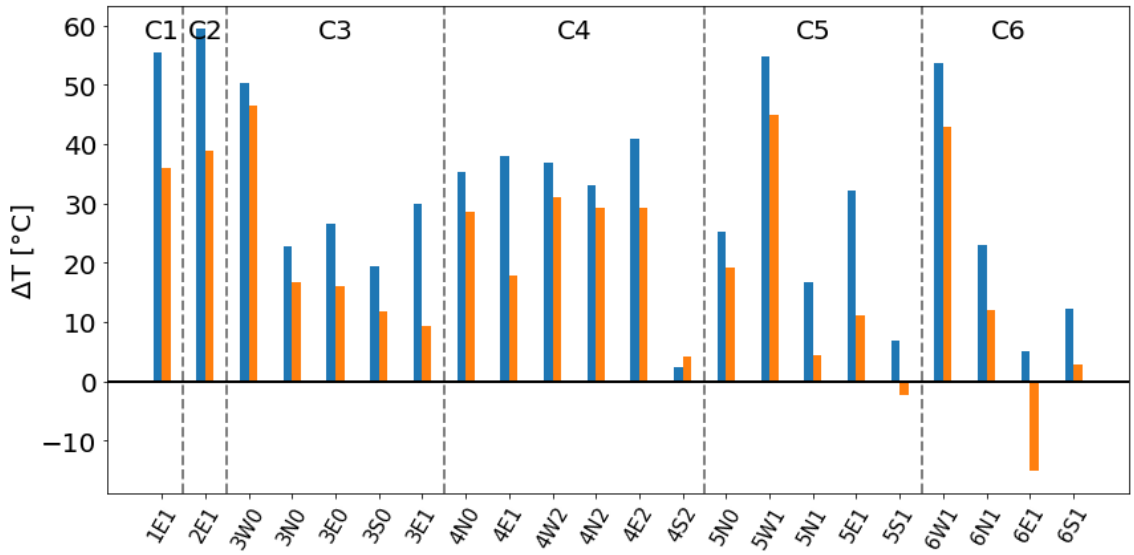

Figure 4.8: Baseline Tuning & Additional Tuning for the RPI

4.2.3 Comparison of Selected Models

Results for case N1, measuring the ΔT, i.e. the difference between the simulation and the experimental values to show the temperature error between the different models.

Table 4.4: Model comparison for Engine 1

	Rohsenow	RPI	BBM
ΔT	53.95	21.35	19.48

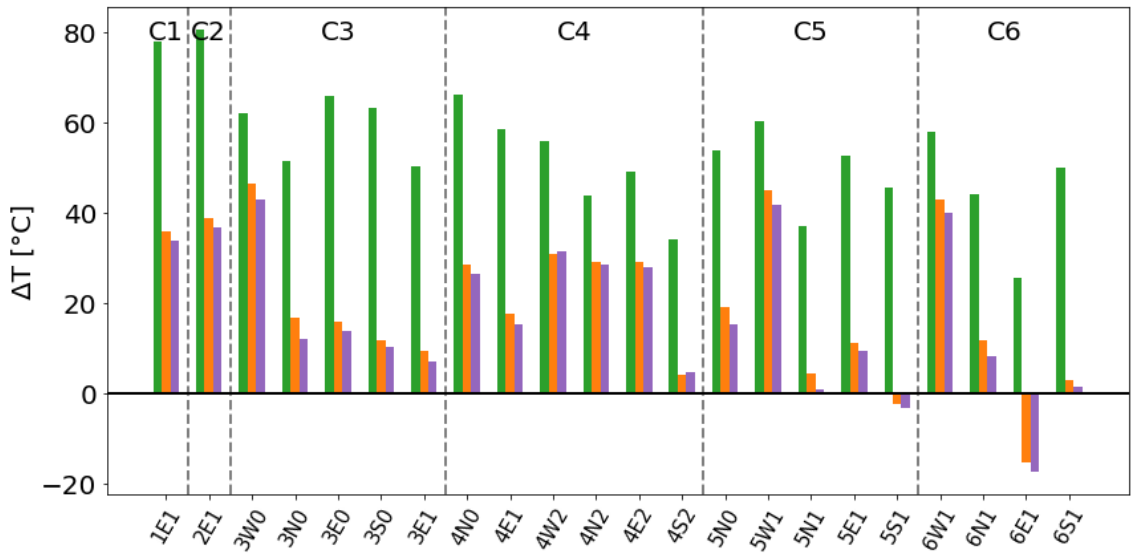

Figure 4.9: Evaluation of Rohsenow, RPI & BBM in various positions in Engine 1

Results for case N2, measuring the ΔT, i.e. the difference between the simulation and the experimental values to show the temperature error between the different models.

Table 4.5: Model comparison for Engine 2

	Rohsenow	**RPI**	**BBM**
ΔT	28.20	17.69	15.29

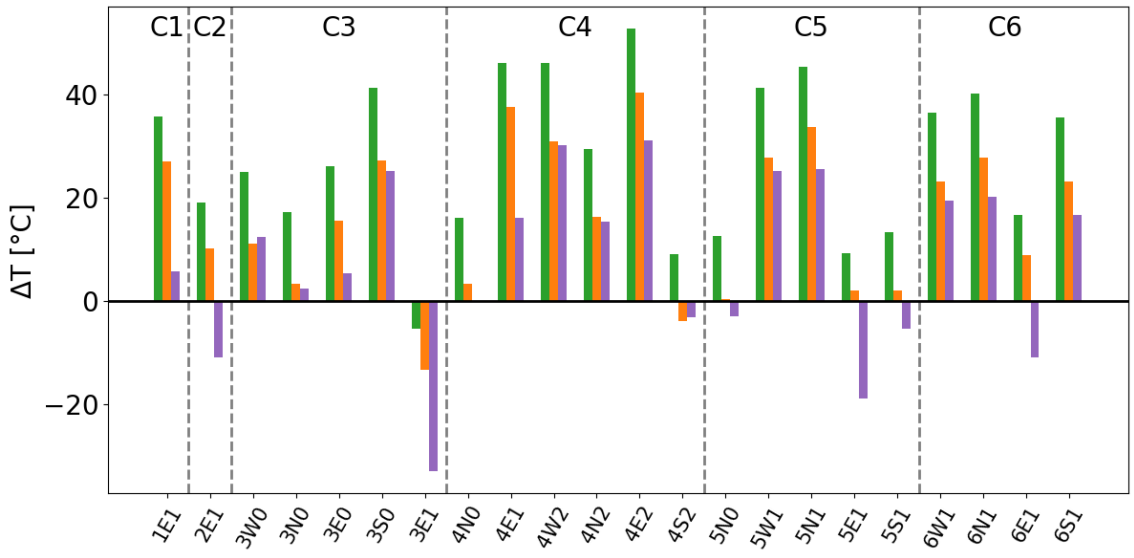

Figure 4.10: Evaluation of Rohsenow, RPI & BBM in various positions in Engine 2

4.2.4 Influence of Pressure & Mass Flow

In the tests a sweep of different coolant mass flow rates and system pressure was performed to study their influence on local nucleate boiling. These operating points were simulated using the BBM. The results of these simulations are compared with those from the tests. Figure 4.11 shows the influence of system pressure on a constant mass flow in the coolant in the BBM framework.

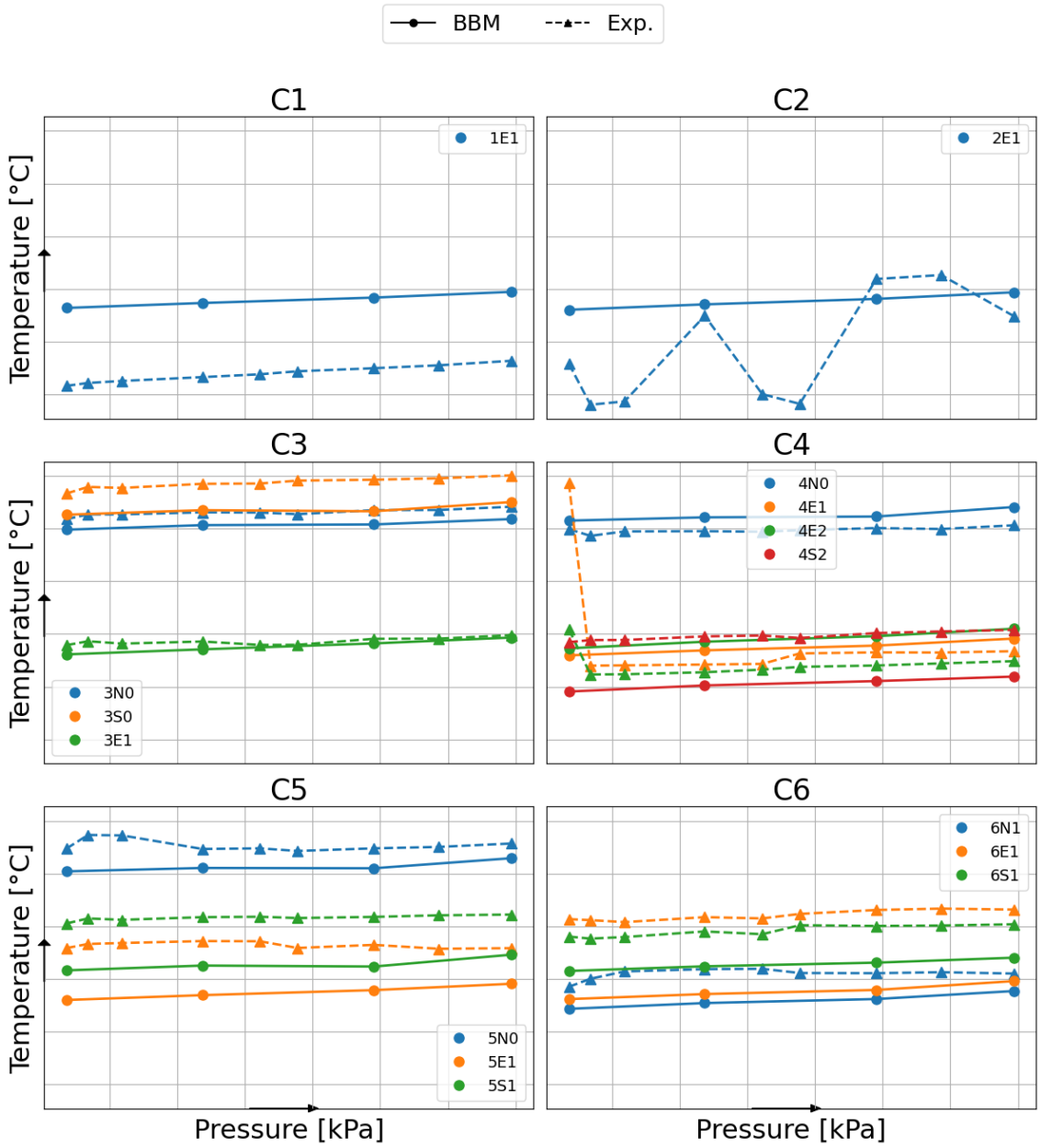

Figure 4.11: BBM: Each subplot shows the results from each of the 6 cylinders in the engine.

Figure 4.12 shows the influence of the mass flow rate on a constant system pressure in the coolant in the BBM framework.

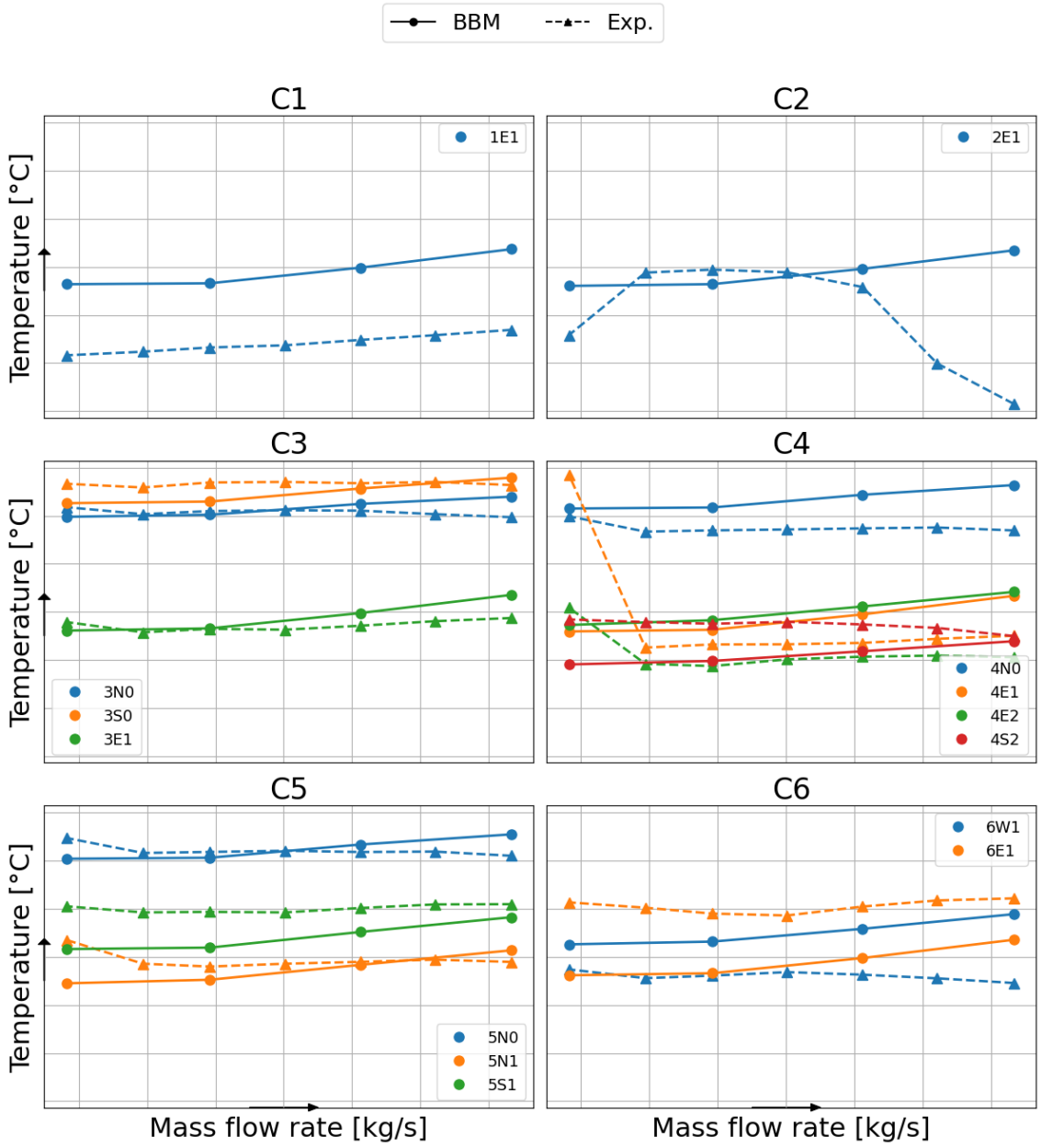

Figure 4.12: BBM: Each subplot shows the results from each of the 6 cylinders in the engine.

Figure 4.13 shows the influence of system pressure on a constant mass flow in the coolant in the DBBM framework.

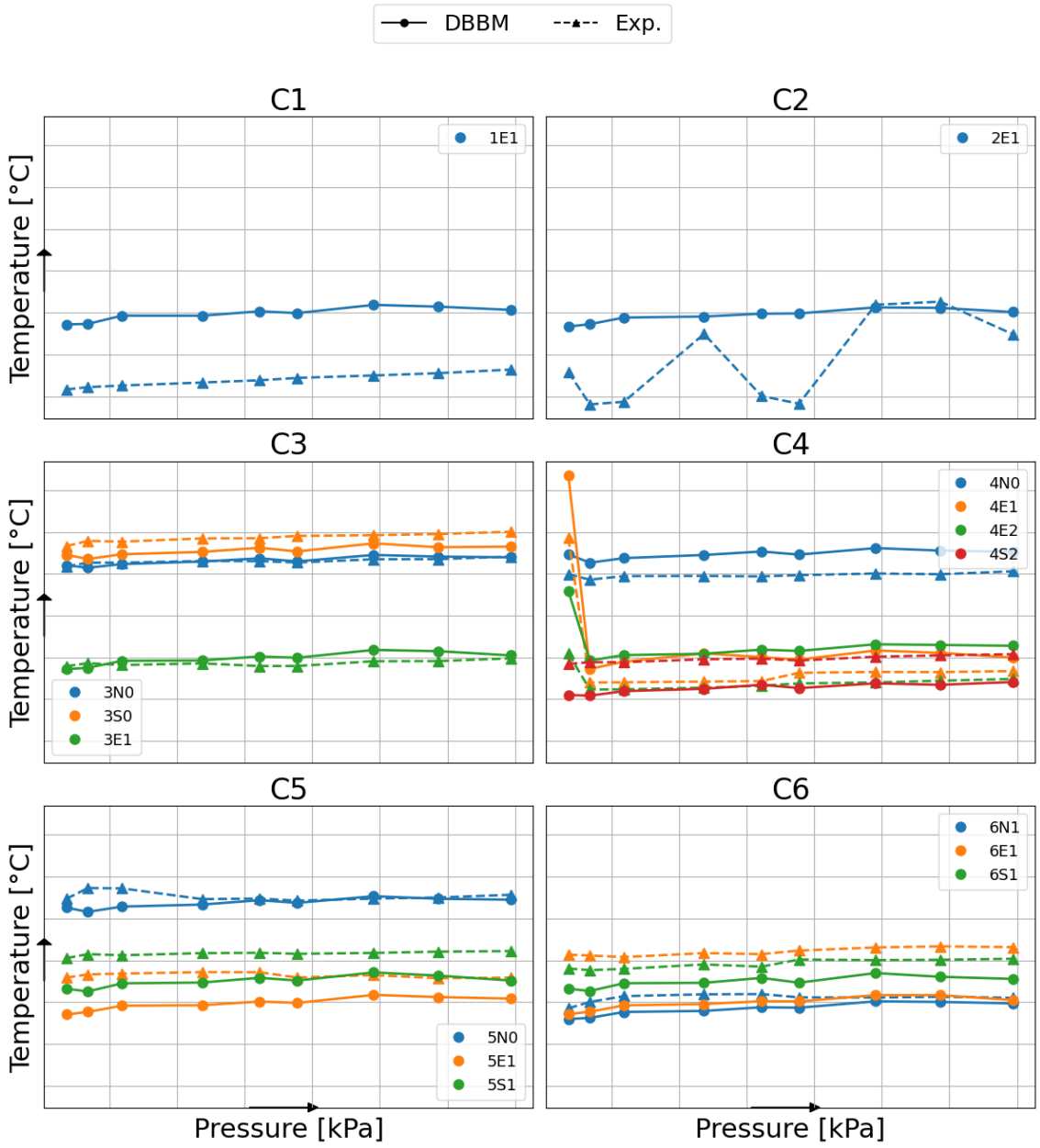

Figure 4.13: DBBM: Each subplot shows the results from each of the 6 cylinders in the engine.

Figure 4.14 shows the influence of the mass flow rate on a constant system pressure in the coolant in the DBBM framework.

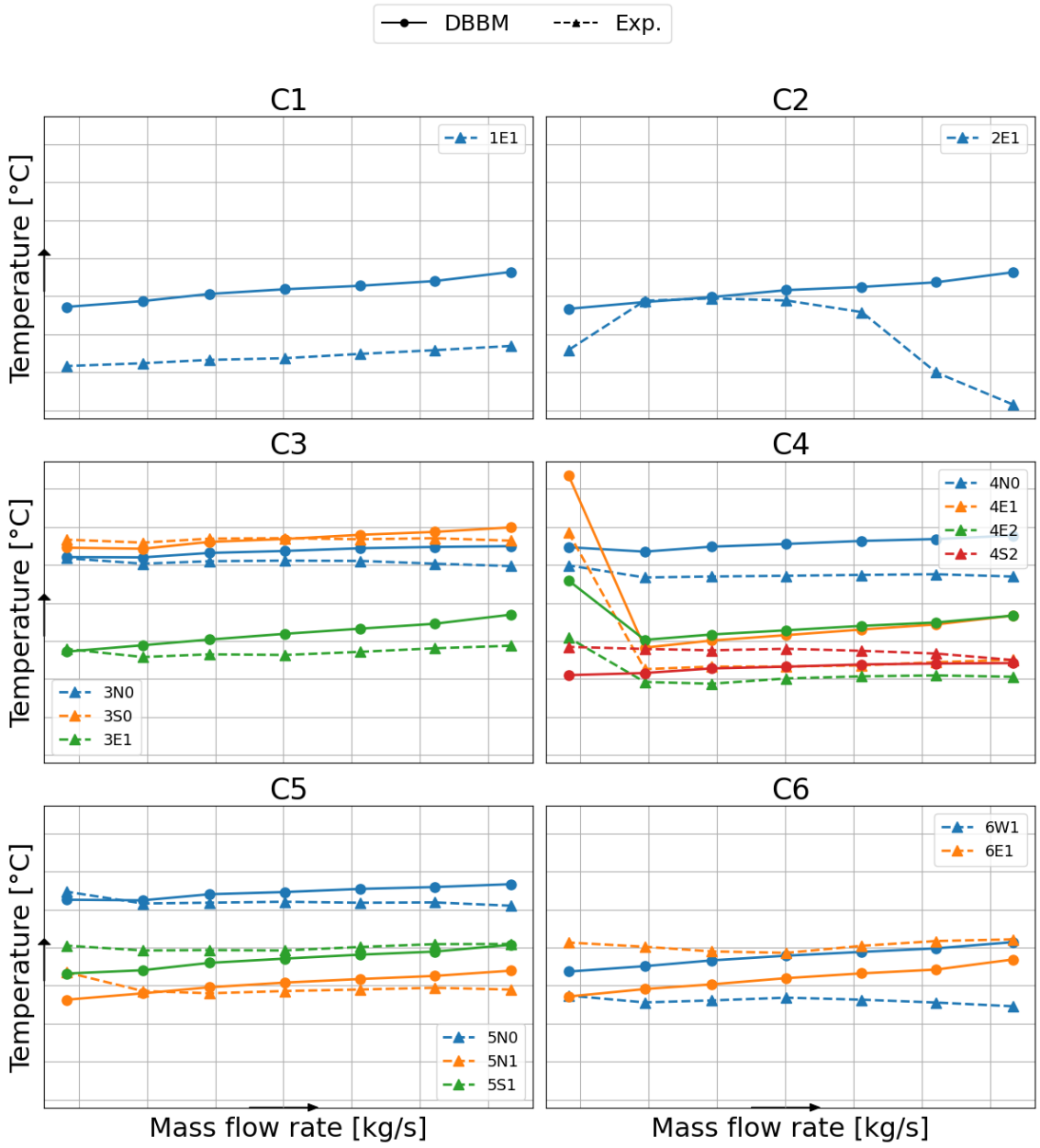

Figure 4.14: DBBM: Each subplot shows the results from each of the 6 cylinders in the engine.

4.2.5 Risk of Film Boiling

Results of spherical observation regions in cylinder 4 in Figure 4.15, measuring the probability (Π_{int}) over the surface area during operating condition P9.

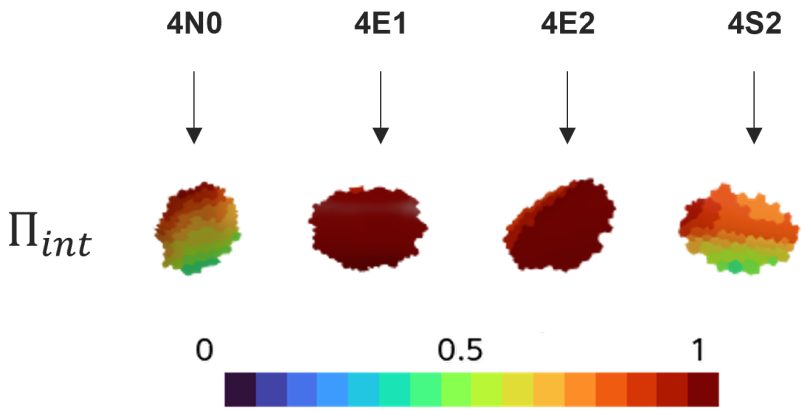

Figure 4.15: Results of Π_{int} in Spherical Observational Regions around Cylinder 4 for Case P9.

Figure 4.16 consists of two subplots for cylinder 4 in the BBM framework. The left subplot illustrates the temperature vs pressure relationship, whereas the right subplot presents the variation of the probability, Π_{int}, with pressure at the corresponding pressure nodes.

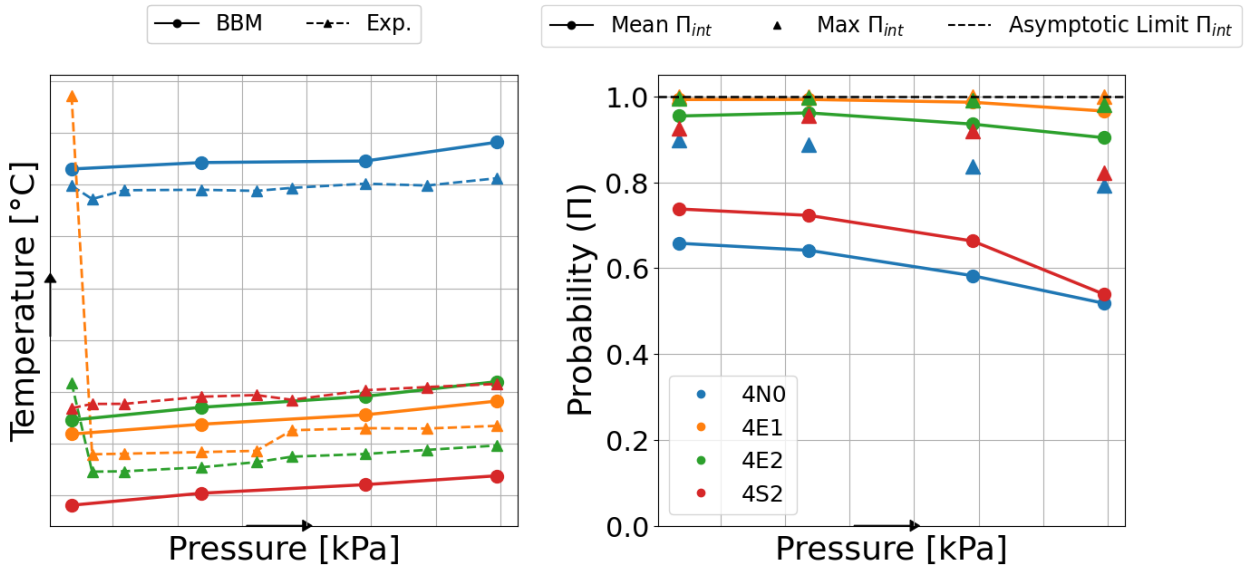

Figure 4.16: Left: Temperature vs Pressure for Case P1 - P9, Right: Probability vs Pressure for Cases P1 - P9.

Figure 4.17 also consists of two subplots for cylinder 4 in the BBM framework. The left subplot illustrates the temperature vs mass flow rate relationship, whereas the right subplot presents the variation of the probability, Π_{int}, with mass flow rate at the corresponding nodes.

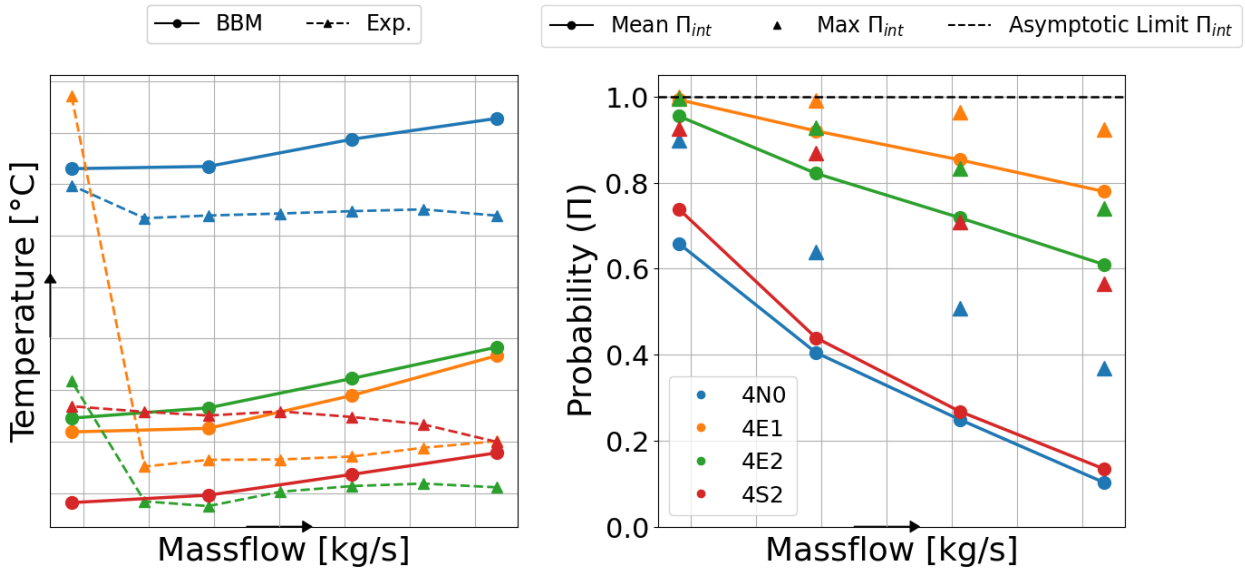

Figure 4.17: Left: Temperature vs Mass flow rate for Case M1 - M7, Right: Probability vs Mass flow rate for Cases M1 - M7.

Probability results (Π_{int}) for probes around cylinder 4 under nominal operating conditions (Case: N1).

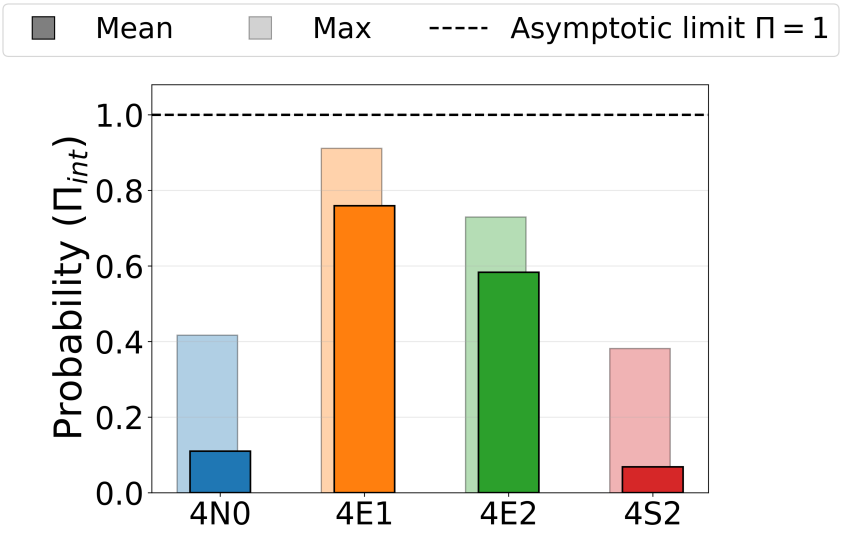

Figure 4.18: Probability Π_{int} Around Cylinder 4 for Nominal Case N1 in BBM.

As discussed in Chapter 3.3.5, probes 4E1 and 4E2 showed clear evidence of film boiling in the experimental data. Figure 4.19 compares the DBBM predictions with the measurements for these probes, located in the exhaust-exhaust bridge of cylinder 4, to assess the model's ability to predict dry-spot and film-boiling temperatures.

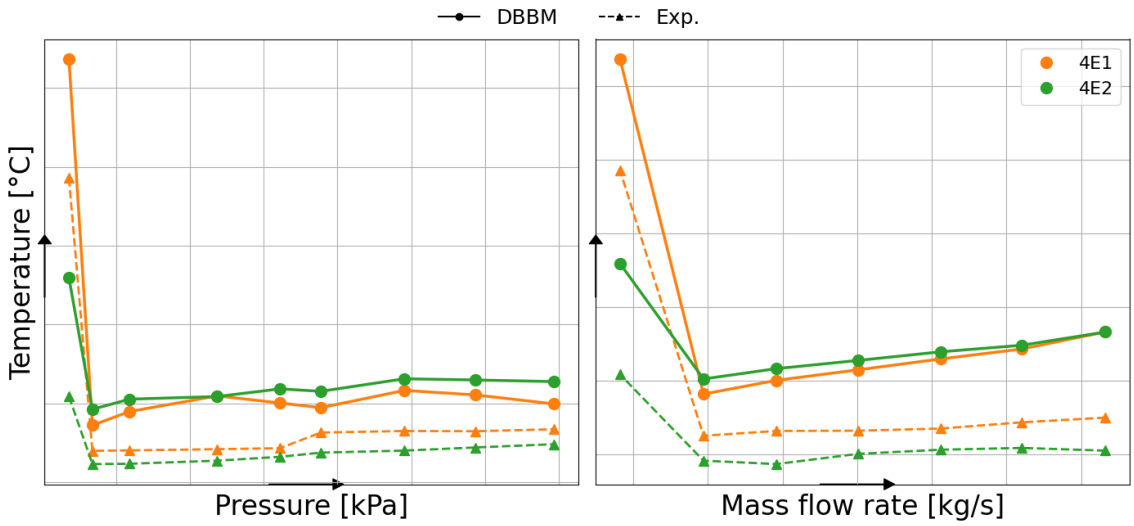

Figure 4.19: Left: Temperature-Pressure for Case P1 - P9, Right: Temperature-Mass flow rate for Cases M1 - M7.

4.2.5.1 Probability of Interaction (Π_{int}) & Dry-spot (Π_{dry})

Figures 4.20 and 4.21 shows the results for the spherical observation regions in cylinder 4 at operating condition P9, illustrating the predicted probabilities of bubble interaction, Π_{int}, and dry-spots, Π_{dry}, across the observational spheres. In the DBBM framework, these probabilities can be compared at different locations within cylinder 4. It provides insight of amount of neighboring bubble interactions occurring within the reference area, in the proximity of the measurement probe. The results therefore indicate whether the local probabilities are approaching the asymptotic limit.

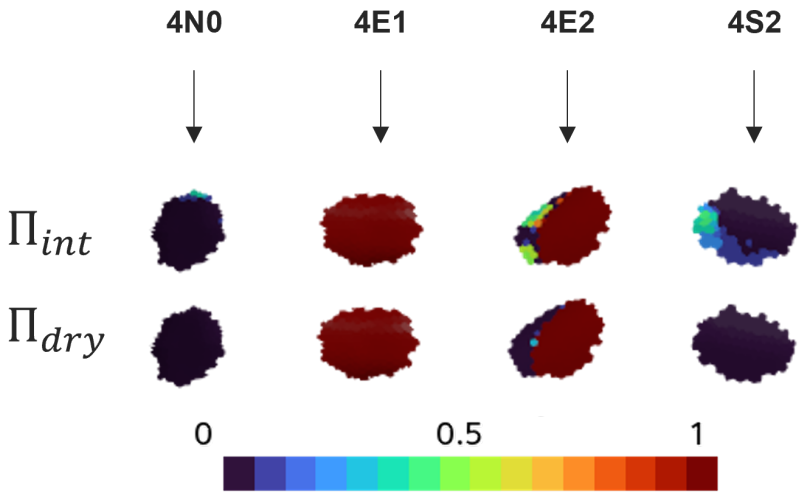

Figure 4.20: Results of Π_{int} & Π_{dry} in Spherical Observational Regions around Cylinder 4 for Case P9.

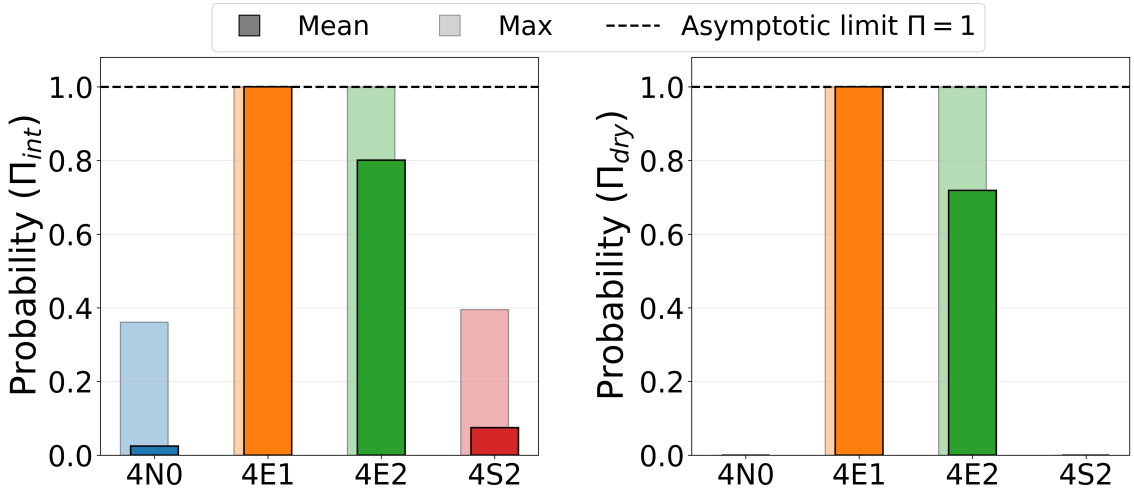

Figure 4.21: Left: Π_{int} around Cylinder 4 for Case P9, Right: Π_{dry} around Cylinder 4 for Case P9

Results of spherical observation regions in cylinders 1 to 6 in the exhaust-exhaust bridge, measuring the probability (Π_{int} and Π_{dry}) over the surface area during operating condition P9.

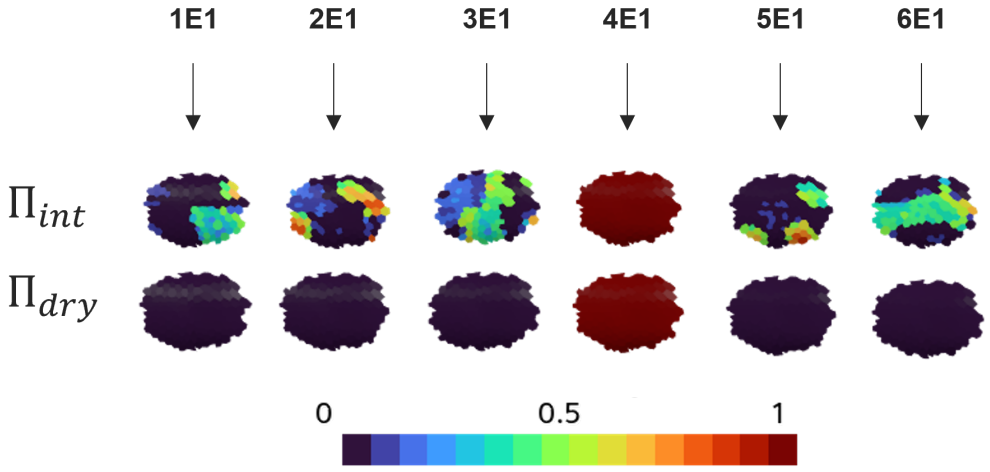

Figure 4.22: Results of Π_{int} & Π_{dry} in Spherical Observational Regions for Cylinder 1 to 6 at exhaust-exhaust bridge for Case P9.

Comparison between the probabilities of interaction (Π_{int}) and dry-spot (Π_{dry}) on cylinders 1 to 6, at their corresponding exhaust-exhaust bridges.

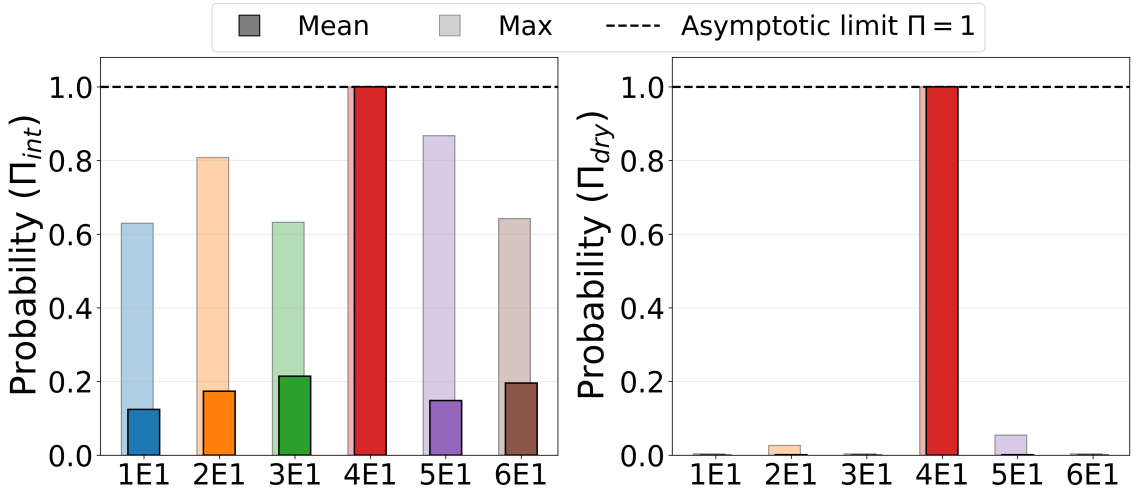

Figure 4.23: Left: Π_{int} at Cylinders 1 to 6 at exhaust-exhaust bridges for Case P9, Right:Π_{dry} at Cylinders 1 to 6 at exhaust-exhaust bridges for Case P9

5
Discussion

In general, The BBM and DBBM showed high potential to predict boiling in the CFD-CHT simulations of the heavy-duty Volvo Diesel engine. Compared to the alternative single-phase and multiphase models implemented in STAR-CCM+ for the engine cases, these models predicted the temperatures with better accuracy compared to the alternative models.

The cell height in the boundary layer had a direct influence on wall temperature. During the simulations, both the wall temperature and stability had to be considered in order to obtain accurate results. An accurate solution was found using a cell height of $1.2mm$. This closely relates to observations by Vasudevan et al. [38] on the height of the near-wall cell, which returned poor accuracy for low y+. The reason was that the vapor bubble diameter was larger than the height of the cell.

Rohsenow's Correlation for the baseline setup showed a non-linear relationship between temperature and heat flux compared to the Forced Convection Heat Transfer (FCHT) model, which only predicts a linear increase in temperature for an increasing heat flux. The difference between the Single-phase and Multiphase implementations of Rohsenow's correlation showed an improvement for the lowest velocity case ($A = 0.46$ m/s). This is because the single phase implementation accounts for the additional heat due to boiling as only sensible heat. Whereas the multiphase implementation accounts for the effects of latent heat-transfer due to nucleation and condensation of vapor bubbles. This effect becomes more significant in low flow velocities, where the vapor bubble population is not negligible. Thus, the multiphase framework gives a more realistic prediction.

The RPI Model was similarly accurate to that of the BBM but was more unstable under lower pressure and mass flow conditions. This happened because the model was over-predicting the volume fraction at the wall. Since RPI models simulate mass transfer at the wall, m_{evap} is directly proportional to the evaporation that transpires at the wall. This means that the vapor fraction produced is proportional to the nucleation site density and bubble departure diameter, which holds no real physical properties of active nucleation sites, but was instead calibrated to match temperatures in the system. This mechanistic approach might not be as applicable for high bubble number density, such as in the FDB regime, where numerous and more complex phenomena are transpiring, as mentioned in 2.1, which are not captured by merely evaluating heat fluxes from quenching and evaporation, as described in the model.

When comparing the different Boiling Departure Lift-off models in Figure 4.3, there was only a small difference in favor of the proposed variant compared to using the Rayleigh-Plesset [23] bubble growth force or Steiner's [13] drag- and lift force. This is because the comparison was made in the BBM framework and since the solution is more prone to be in the FDB regime compared to isolated bubbles, all three models gravitate towards the same solution and only slightly deviate in cases with a low probability of bubble interaction (Π_{int}).

The sensitivity of the estimated temperatures to different model parameters, such as b, C_{sf}, and N_0, in the BBM was studied. The b-parameter affects the bubble growth constant and thus influences the BDL part of the BBM and also the probability of bubble interaction (π_{int}). With increasing values of b, the bubble departure diameter increases; however, it also indirectly decreases the number of active sites (N_{avg}). So there will be a balance between larger but fewer bubbles; or smaller but an increased number of bubbles. These unique solutions give similar results in Figure 4.4, except for the case with the growth of the smallest bubbles ($b = 0.02$). The C_{sf}-parameter governs the FDB heat flux through the Rohsenow's correlation, increasing the C_{sf} results in a lower heat flux in the FDB regime and thereby higher wall temperatures. The parameter N_0 determines the number of active nucleation sites and thus impacts the probability of bubble interaction, Π_{int}. The higher the number, the more bubble interactions will be present. Increasing it further than ($N_0 = 5e5$) provides only a slight decrease in temperature, this is because the solution has already reached its asymptote ($\Pi_{int} = 1$). Having a lower value increases the influence of the BDL sub-model and in this case, resulted in higher deviation from the test results.

It should also be noted that the calibration has been carried out using the current convective boundary conditions derived from the *Converge CFD* combustion simulations. Consequently, any improvement in the accuracy of the combustion simulations may contribute to a more accurate and robust calibration procedure.

The different values for the empirical constants in the BBM were evaluated for CFD-CHT simulations of the HDD. These additional evaluations helped improve the accuracy of the model. The material-fluid interactions between the different cases differ to some extent, such as the composition of the coolant mixture and the previously mentioned uncertainties in surface roughness. The model was significantly improved in the N1 case by decreasing the C_{sf}-parameter and increasing the N_0-parameter, resulting in a decrease in the average error in the predicted temperature from 38.3° to 27.63°, as shown in Figure 4.7.

Since the parameters of the RPI model directly affect the heat flux components, unlike in the BBM, where a probability function is used to blend the different boiling heat flux formulations, the empirical parameters in the model directly influence the intensity of the boiling heat flux.

The calibrated values of N0 and b provided results in good agreement with the experimental data for the baseline academic case. However, the same values resulted in excessive vapor buildup under certain critical conditions in the engine simulations, resulting in numerical instabilities. Although increasing these two parameters is practical, the result causes a nonphysical increase in interphase mass transfer at the heated wall-liquid interface. Any improvement in this regard should involve calibrating the empirical constants, such as A and B in the formulation for active nucleation site density proposed by Lemmert and Chawla [32] which adds another non-linear effect to calculating the active nucleation site density. This would still not be sufficient to fix the issue of mass transfer produced at the wall. Thus, it is necessary to calibrate the wall heat flux based of individual bubbles using parameters such as K_{quench} and C_w. Changing these parameters might lead to better accuracy, but the solver diverges from its physical representation when modifying the parameters from their experimentally suited constants.

Comparisons of selected models contain the in-built single-phase Rohsenow Correlation, the in-built proposed RPI model and the manually implemented proposed BBM. These comparisons were made for both nominal cases (N1 and N2) for engine models 1 and 2, respectively. The results show that the BBM outperforms the alternative models for both engine models. Although the ease of use of Rohsenow's correlation is certainly beneficial, the correlation made for pool boiling is not suitable for large-scale HDD applications where flow boiling is much more prevalent. Using the RPI model for these large-scale applications, compared to the BBM, differs mostly in regions of high superheated temperatures. although there are similarities in baseline. Since the DBBM and the BBM showed similar results, the same conclusion can be drawn that the DBBM outperforms the other models and also provides the possibility of estimating the heat flux beyond the critical heat flux.

For the pressure sweep, the three cases (P1, P2 and P3) contain a lower pressure than the nominal case (N1), with a constant mass flow rate. These three cases were used to evaluate the influence of operating pressure of the cooling system on the temperature of the solid parts of the engine. The general trend predicts a lower temperature with decreasing pressure because the decrease in pressure decreases the saturation temperature of the liquid, thereby resulting in more nucleate boiling. An increase in nucleate boiling results in enhanced heat transfer, which in turn lowers the temperature of the engine. However, a further reduction in system pressure lead to occurrence of transition boiling, evidenced by an increase in temperature close to cylinder 4. This happens in the experiment only in cylinder 4. A closer look at cylinder 4 in Figure 4.11, shows that the experimental values in probes 4E1 and 4E2, for the lowest pressure case (P9), have a significant increase in temperatures. This is attributed to accumulation of vapor, resulting in the formation of dry plots, which eventually led to the occurrence of transition boiling and it is observed only at the exhaust-exhaust bridge. This phenomenon was also observed when the mass flow rate of the coolant was decreased in steps. The occurrence of transition boiling was observed for the operating condition with the lowest mass flow rate, as shown in Figure 4.12. A decrease in mass flow rate decreases both the forced convection

heat transfer and the flow induced suppression of nucleate boiling, both resulting in increased nucleate boiling.

The risk of film boiling, when using the BBM, is quantified with its probability of bubble interaction (Π_{int}). This was done in two regions: around cylinder 4, in two probes, 4E1 and 4E2, placed adjacent to each other in the exhaust-exhaust bridge of Cylinder 4. A higher Π_{int} was observed in cylinder 4, especially between the exhaust-exhaust bridge. The contours of the probability of bubble interaction shown in Figure 4.15 and the plot of the probability of bubble interaction as a function of pressure shown in Figure 4.16 show the quantified risk of the occurrence of transition boiling. The model predicts $\Pi_{int} = 1$, where the increased temperatures were located and notably in Figure 4.18, which is the nominal case (N1), Π_{int} stays below one, since there is no transition or film boiling under normal operating conditions.

The Dry-spot Blended Boiling Model (DBBM), using an additional probability (Π_{dry}), to account for probability of dry-spots, does provide a solution with increased temperature for the lowest pressure, this is observed in Figure 4.13. Further tuning was needed to achieve this, by reducing the reference active nucleation site number (N_0). The model, in its current state, slightly over-predicts temperature. A more detailed examination of cylinder 4 in Figure 4.19 shows that both probes on the exhaust-exhaust bridge (4E1 and 4E2) resulted in a higher predicted temperature, compared to experimental values. One of the possible reasons for this could be due to how the q_{dry} is modeled. The over-prediction of dry conditions is suspected to be due to the model neglecting the spatial arrangements of the surrounding bubbles, and only assumes the presence of five or more bubbles to indicate dry-spot formation. This implies that no bulk liquid can be supplied to the microlayer beneath the bubble located at the center. However, in reality, the presence of five or more surrounding bubbles is not always equidistant or symmetrically distributed around the center bubble and may instead be highly skewed or non-uniform. Since the model does not resolve geometric variations in bubble distribution, as a consequence, the model may over-predict the occurrence of dry-spots. Despite this limitation, this criterion provides a simple basis for identifying conditions under which dry-spots are assumed to occur and is deemed capable of predicting with sufficient accuracy.

The comparison between Π_{int} and Π_{dry} in Figures 4.21 and 4.23 highlights the distinct physical meanings of the two probabilities. The former is defined as the occurrence of more than 1 bubble interaction in a defined area, whereas the latter corresponds to the occurrence of more than 5 bubbles within the same defined area. This stricter criterion of Π_{dry} represents a more intense boiling condition and, therefore, is less sensitive to the onset of interaction, but more indicative of regions where boiling has become locally intense. Accordingly, Π_{int} is primarily useful for identifying the initiation and onset of bubble interaction, while Π_{dry} provides additional information on the progression of the boiling process beyond the initial nucleate boiling regimes. In particular, Π_{dry} serves as a higher contrast indicator of severe local conditions beyond the fully developed regime (FDB), thus offering further insight

into the extent of developed boiling and the likelihood of occurrence of dry-spots. This thermal feedback, as Π_{dry} significantly reduces local heat transfer, leads to higher wall temperatures, which in turn promote vapor accumulation and reinforce dry-spots.

6
Conclusion

The numerical simulations, when compared with the experimental measurements, were used to validate the Blended Boiling Model (BBM) and the Dry-spot Blended Boiling Model (DBBM) for two heavy-duty diesel engine variants. Overall, both models predict the boiling heat flux under the investigated operating conditions with good accuracy, considering the uncertainties associated with the experiments and the numerical framework. The agreement obtained between simulations and measurements is attributable to the model calibration and fine tuning of empirical constants involved in the models.

A key outcome of the study is the ability of the model to estimate the local heat transfer phenomena, especially in regions exposed to intensive boiling, particularly in the exhaust-exhaust bridge. The experimental data indicate high-intensity boiling under the most demanding conditions and in these cases, the BBM is not able to reproduce the corresponding elevated wall temperatures. However, it includes the probability of bubble interaction parameter (Π_{int}) to quantify the intensity of boiling and the limits of the partial boiling regime, However the BBM does not provide direct information on proximity to critical heat flux or transition boiling.

By extending the framework with the probability of dry-spots (Π_{dry}), the DBBM is able to capture, with reasonably good accuracy, the temperature rise observed at the lowest pressure and mass flow rate conditions. In this way, the DBBM effectively extends the applicability of the original BBM into the transitional boiling regime by switching between the BBM heat flux and a heat flux defined for the single phase vapor according to the predicted probability of occurrence of dry-spots. This makes the DBBM a more suitable tool when the objective is not only to identify the onset of intensive boiling, but also to represent the deterioration in heat transfer associated with transition towards film boiling conditions.

The other wall-boiling models available in STAR-CCM+, including the single-phase Rohsenow correlation and the RPI model, provide simpler alternatives for predicting boiling heat flux. However, in the present study, they show lower accuracy compared to BBM and DBBM against the experimental results. Their main advantage lies in their ease of implementation and lower setup effort, which may still make them useful in applications where detailed and accurate resolution of boiling phenomena is not required.

In summary, the BBM and especially the DBBM provide a useful numerical method-

ology for analyzing subcooled boiling in heavy-duty engine coolant jackets. The BBM offers a practical indication of boiling intensity and the limits of safe partial boiling, while the DBBM improves the predictive capabilities in more severe conditions by accounting for dry-spots. These features make the models valuable tools for the development of advanced engine cooling strategies, particularly where controlled boiling is of interest.

Bibliography

[1] H. Steiner, G. Brenn, F. Ramstorfer, and B. Breitschädel, "Increased cooling power with nucleate boiling flow in automotive engine applications," in *Proceedings of the 13th International Heat Transfer Conference (IHTC-13)*, Sydney, Australia: Begell House Inc., 2006. DOI: 10.1615/IHTC13.p13.120.

[2] H. Punekar and S. Das, "Numerical simulation of subcooled nucleate boiling in cooling jacket of ic engine," SAE Technical Paper, Tech. Rep. 2013-01-1651, 2013. DOI: 10.4271/2013-01-1651. [Online]. Available: https://doi.org/10.4271/2013-01-1651.

[3] J. C. Chen, "Correlation for boiling heat transfer to saturated fluids in convective flow," *Industrial & Engineering Chemistry Process Design and Development*, vol. 5, no. 3, pp. 322–329, 1966. DOI: 10.1021/i260019a023.

[4] M. Shala, "Simulation of nucleate boiling flow using a multiphase mixture modelling approach," *IMA Journal of Applied Mathematics*, vol. 77, no. 1, pp. 47–58, 2012.

[5] N. Kurul and M. Z. Podowski, "Multidimensional effects in sub-cooled boiling," in *Proceedings of the Ninth Heat Transfer Conference*, Jerusalem, 1990.

[6] S. Hua, R. Huang, and P. Zhou, "Numerical investigation of two-phase flow characteristics of subcooled boiling in ic engine cooling passages using a new 3d two-fluid model," *Applied Thermal Engineering*, vol. 90, pp. 648–663, 2015. DOI: 10.1016/j.applthermaleng.2015.07.037.

[7] I. C. Finlay, R. J. Boyle, J. P. Pirault, and T. Biddulph, "Nucleate and film boiling of engine coolants flowing in a uniformly heated duct of small cross section," SAE International, SAE Technical Paper 870032, 1987.

[8] F. Ramstorfer, H. Steiner, G. Brenn, C. Kormann, F. Rammer, et al., "Subcooled boiling flow heat transfer from plain and enhanced surfaces in automotive applications," *Journal of Heat Transfer*, vol. 130, no. 1, pp. 81–99, 2008.

[9] Z. Chen, F. Wu, and Y. Utaka, "Numerical simulation of thermal property effect of heat transfer plate on bubble growth with microlayer evaporation during nucleate pool boiling," *International Journal of Heat and Mass Transfer*, vol. 118, pp. 989–996, 2018.

[10] S. Vasudevan, "Subcooled boiling flow in liquid-cooled internal combustion engines," Doktorsavhandlingar vid Chalmers tekniska högskola, Ny serie nr. 5171, Ph.D. dissertation, Chalmers University of Technology, Göteborg, Sweden, 2022, ISBN: 978-91-7905-705-3.

[11] T. Sato and H. Matsumura, "On the conditions of incipient subcooled-boiling with forced convection," *Bulletin of JSME*, vol. 7, no. 26, pp. 392–398, 1964. DOI: 10.1299/jsme1958.7.392.

[12] W. M. Rohsenow, "A method of correlating heat transfer data for surface boiling of liquids," Massachusetts Institute of Technology, Division of Industrial Cooperation, Cambridge, MA, Technical Report Technical Report No. 5, Jul. 1951, Contract N5ori-07827, NR-035-267, D.I.C. Project Number 6627. Presented at ASME Annual Meeting, Nov. 1951.

[13] H. Steiner, A. Kobor, and L. Gebhard, "A wall heat transfer model for subcooled boiling flow," *International Journal of Heat and Mass Transfer*, vol. 48, no. 19-20, pp. 4161–4173, 2005. DOI: 10.1016/j.ijheatmasstransfer.2005.04.016.

[14] F. W. Dittus and L. M. K. Boelter, "Heat transfer in automobile radiators of the tubular type," *University of California Publications in Engineering*, vol. 2, no. 13, pp. 443–461, 1930, Reprinted in International Communications in Heat and Mass Transfer, vol. 12, no. 1, pp. 3-22, 1985.

[15] H. K. Forster and N. Zuber, "Dynamics of vapor bubbles and boiling heat transfer," *AIChE Journal*, vol. 1, no. 4, pp. 531–535, 1955. DOI: 10.1002/aic.690010425.

[16] J. F. Klausner, R. Mei, D. M. Bernhard, and L. Z. Zeng, "Vapor bubble departure in forced convection boiling," *International Journal of Heat and Mass Transfer*, vol. 36, no. 3, pp. 651–662, 1993. DOI: 10.1016/0017-9310(93)80041-R.

[17] J. R. Wiebe and R. L. Judd, "Superheat layer thickness measurements in saturated and subcooled nucleate boiling," *Journal of Heat Transfer*, vol. 93, no. 4, pp. 455–461, 1971. DOI: 10.1115/1.3449845.

[18] T. Mazzocco, W. Ambrosini, R. Kommajosyula, and E. Baglietto, "A reassessed model for mechanistic prediction of bubble departure and lift off diameters," *International Journal of Heat and Mass Transfer*, vol. 117, pp. 119–124, 2018. DOI: 10.1016/j.ijheatmasstransfer.2017.09.105.

[19] L. Z. Zeng, J. F. Klausner, D. M. Bernhard, and R. Mei, "A unified model for the prediction of bubble detachment diameters in boiling systems–ii. flow boiling," *International Journal of Heat and Mass Transfer*, vol. 36, no. 9, pp. 2271–2279, 1993. DOI: 10.1016/S0017-9310(05)80111-1.

[20] N. Zuber, "The dynamics of vapor bubbles in nonuniform temperature fields," *International Journal of Heat and Mass Transfer*, vol. 2, no. 1–2, pp. 83–98, 1961. DOI: 10.1016/0017-9310(61)90016-1.

[21] D. Legendre and J. Magnaudet, "A note on the lift force on a spherical bubble or drop in a low-reynolds-number shear flow," *Physics of Fluids*, vol. 9, no. 11, pp. 3572–3574, 1997. DOI: 10.1063/1.869466.

[22] M. G. Cooper and A. J. P. Lloyd, "The microlayer in nucleate pool boiling," *International Journal of Heat and Mass Transfer*, vol. 12, no. 8, pp. 895–913, 1969. DOI: 10.1016/0017-9310(69)90154-9.

[23] M. S. Plesset and S. A. Zwick, "The growth of vapor bubbles in superheated liquids," *Journal of Applied Physics*, vol. 25, no. 4, pp. 493–500, 1954. DOI: 10.1063/1.1721668.

[24] S. Vasudevan, S. Etemad, L. Davidson, and G. M. Villar, "Numerical model to estimate subcooled flow boiling heat flux and to indicate vapor bubble interaction," *International Journal of Heat and Mass Transfer*, vol. 170, p. 121 038, 2021. DOI: 10.1016/j.ijheatmasstransfer.2021.121038.

[25] Q. Li, Y. Jiao, M. Avramova, P. Chen, J. Yu, J. Chen, and J. Hou, "Development, verification and application of a new model for active nucleation site density in boiling systems," *Nuclear Engineering and Design*, vol. 328, pp. 1–9, 2018. DOI: 10.1016/j.nucengdes.2017.12.030.

[26] S. J. Ha and H. C. No, "A dry-spot model of critical heat flux in pool and forced convection boiling," *International Journal of Heat and Mass Transfer*, vol. 41, no. 2, pp. 303–311, 1997. DOI: 10.1016/S0017-9310(97)00139-3.

[27] B. Tao, "CFD homogeneous mixing flow modelling to simulate subcooled nucleate boiling flow," SAE International, SAE Technical Paper 2004-01-1510, 2004. DOI: 10.4271/2004-01-1510.

[28] Siemens Digital Industries Software, *Simcenter STAR-CCM+ user guide*, Version 2024.1, Available from Siemens Support Center, Siemens Digital Industries Software, Plano, TX, USA, 2024.

[29] M. V. H. Del Valle and D. B. R. Kenning, "Subcooled flow boiling at high heat flux," *International Journal of Heat and Mass Transfer*, vol. 28, no. 10, pp. 1907–1920, 1985.

[30] G. C. Bartolomei and V. M. Chanturiya, "Experimental study of true void fraction when boiling subcooled water in vertical tubes," *Thermal Engineering*, vol. 14, no. 2, pp. 123–128, 1967.

[31] R. Cole, "A photographic study of pool boiling in the region of the critical heat flux," *AIChE Journal*, vol. 6, no. 4, pp. 533–542, 1960. DOI: 10.1002/aic.690060405.

[32] M. Lemmert and J. M. Chawla, "Influence of flow velocity on surface boiling heat transfer coefficient," in *Heat Transfer in Boiling*, E. Hahne and U. Grigull, Eds., New York, NY, USA: Academic Press and Hemisphere, 1977, pp. 237–247.

[33] Siemens Digital Industries Software, *Simcenter STAR-CCM+ user guide*, Version 2024.1, Section: Nucleation Site Number Density Models. Available from Siemens Support Center, Siemens Digital Industries Software, Plano, TX, USA, 2024.

[34] J. Weisman and B. S. Pei, "Prediction of critical heat flux in flow boiling at low qualities," *International Journal of Heat and Mass Transfer*, vol. 26, no. 10, pp. 1463–1477, 1983. DOI: 10.1016/S0017-9310(83)80048-8.

[35] M. Gholinia, A. A. Ranjbar, D. D. Ganji, and M. Pourfallah, "Experimental analysis of subcooled flow boiling heat flux on gray cast iron block in heavy-duty diesel engine-like conditions: Optimization using central composite design," *International Journal of Engineering, Transactions B: Applications*, vol. 37, no. 11, pp. 2288–2302, Nov. 2024. DOI: 10.5829/ije.2024.37.116.14. [Online]. Available: www.ije.ir.

[36] V. I. Tolubinskiy and D. M. Kostanchuk, "Vapour bubbles growth rate and heat transfer intensity at subcooled water boiling," in *International Heat Trans-*

fer Conference 4, vol. 5, Paris, France: Elsevier, 1970, B2.8. DOI: 10.1615/IHTC4.250.

[37] Siemens Digital Industries Software, "Under-relaxation of boiling heat flux in Simcenter STAR-CCM+," *Simcenter STAR-CCM+ Knowledge Base*, 2024.

[38] S. Vasudevan, S. Etemad, L. Davidson, and M. Bovo, "Comparative analysis of single and multiphase numerical frameworks for subcooled boiling flow in an internal combustion engine coolant jacket," *Applied Thermal Engineering*, vol. 219, p. 119 435, 2023. DOI: 10.1016/j.applthermaleng.2022.119435.

A

Appendix 1

The user defined coefficients are set as in Eq. A.1 with all terms bundled into the first term (A_{user}).

$$\begin{aligned} A_{user} &= q_{UR} + B_{fc}T_c + C_{fc}T_w \\ B_{user} &= 0 \\ C_{user} &= 0 \\ D_{user} &= 0 \end{aligned} \tag{A.1}$$

And since it is not possible to change the internal coefficients directly, however, the expressions representing the internal coefficients can be used and included in the user defined coefficients. it is therefore possible to remove the internal coefficients as follows:

$$\begin{aligned} B_{fc} &= \begin{cases} -B_{internal} + (1-\Pi)B_{internal}, & T > T_{sat} \\ 0, & T < T_{sat} \end{cases} \\ C_{fc} &= \begin{cases} -C_{internal} + (1-\Pi)C_{internal}, & T > T_{sat} \\ 0, & T < T_{sat} \end{cases} \end{aligned} \tag{A.2}$$

Where q_{UR} is the under-relaxed heat flux.

DEPARTMENT OF MECHANICS AND MARITIME SCIENCES
CHALMERS UNIVERSITY OF TECHNOLOGY
Gothenburg, Sweden 2026
www.chalmers.se

CHALMERS
UNIVERSITY OF TECHNOLOGY